UNIVERSITY OF OKLAHOMA

GRADUATE COLLEGE

FULL ANISOTROPIC MODEL FOR SIMULATING THE INFRARED REFLECTION ABSORPTION SPECTRA (IRRAS) OF SELF-ASSEMBLED MONOLAYERS (SAMS) FROM ALL-ATOM MOLECULAR DYNAMICS SIMULATIONS

A THESIS

SUBMITTED TO THE GRADUATE FACULTY

in partial fulfillment of the requirements for the

Degree of

MASTER OF SCIENCE

By

NAFISA AMIN
Norman, Oklahoma
2020

Downloaded from SHAREOK. Persistent Handle URL: https://hdl.handle.net/11244/324841

FULL ANISOTROPIC MODEL FOR SIMULATING THE INFRARED REFLECTION ABSORPTION SPECTRA (IRRAS) OF SELF-ASSEMBLED MONOLAYERS (SAMS) FROM ALL-ATOM MOLECULAR DYNAMICS SIMULATIONS

A THESIS APPROVED FOR THE HOMER L. DODGE DEPARTMENT OF PHYSICS AND ASTRONOMY

BY THE COMMITTEE CONSISTING OF

Dr. Lloyd A. Bumm, Chair

Dr. Michael B. Santos

Dr. Arne Schwettmann

© Copyright by NAFISA AMIN 2020
All Rights Reserved

Acknowledgements

I would like to express my sincere gratitude to my adviser Dr. Lloyd A. Bumm for the direction, invaluable guidance, and unconditional support throughout my research. Through all the tremendous effort Dr. Bumm spent on me, I improved myself greatly in many aspects, of which the most significant is the research attitude—never stop challenging myself. All the training and improvements will benefit me in the future work. I thank my committee members Dr. Lloyd Bumm, Dr. Michael Santos and Dr. Arne Schwettmann for their support and valuable suggestions. I would also like to extend my gratitude to Soumya Bhattacharya and Mitchell P. Yothers for sharing their expertise and their selfless contribution towards my degree. Finally, I would like to thank my parents, sister and my beloved husband for their constant encouragement, endless support and love throughout my life and my academic career.

Abstract

It is important to understand the internal molecular structure of molecular monolayers because that determines the physical and chemical properties of their surface. Infrared spectroscopy is a powerful method to measure the molecular orientation, but to fully harness the information, the spectra need to be compared to structural models. A full anisotropic model is established for simulating the infrared reflection absorption spectra (IRRAS) of self-assembled monolayers (SAMs) based on the methods of Allara and Parikh. The primary focus is to bridge the molecular structures from molecular dynamics simulations with the experimental spectra. The methylene and methyl group orientation are used in the simulations to calculate the complex refractive index tensors in the mid infrared (MIR) using experimental data from a reference phase. The Kramers-Kronig relation is used to calculate the frequency dependent refractive index tensor in the MIR from the absorption of each mode. The high frequency part of the refractive index tensor is calculated from atomic bond vectors in the simulation based on the bond polarizabilities. Afterwards, the IRRAS spectra can be computed using the 4×4 transfer matrix method. Finally, the IRRAS spectra of MD simulation results based on proposed SAM structures are compared.

Table of Contents

ACKNOWLEDGEMENTS **IV**

ABSTRACT **V**

TABLE OF CONTENTS **VI**

1 INTRODUCTION **1**

1.1 MOTIVATION 1
1.2 OVERVIEW OF INFRARED REFLECTION ABSORPTION SPECTROSCOPY (IRRAS) 2
1.3 OVERVIEW OF THE PROJECT 5
1.4 REFERENCE 6

2 CONSTRUCTION OF THE COMPLEX REFRACTIVE INDEX TENSOR **9**

2.1 COMPLEX REFRACTIVE INDEX TENSOR 9
2.1.1 Electromagnetic Wave Propagation and Absorption 11
2.1.2 Refractive Index Tensor in Anisotropic Medium 12
2.2 THE KRAMERS-KRONIG RELATION 14
2.2.1 Calculation of Refractive Index from the Absorption Spectrum 14
2.2.2 Dielectric Dispersion and Frequency Response Regions 15
2.3 REFERENCES 16

3 ANALYTIC FUNCTION KRAMERS-KRONIG TRANSFORM PAIRS **18**

3.1 GENERAL OVERVIEW OF KRAMERS-KRONIG RELATION 18
3.2 THE KRAMERS-KRONIG INTEGRAL 19
3.3 NUMERICAL KRAMERS-KRONIG INTEGRATION APPROXIMATION 21
3.4 ABSORPTION LINE SHAPE MODELS 21
3.5 DECOMPOSITION OF THE ABSORPTION SPECTRUM 24
3.6 VERIFICATION OF THE ANALYTIC FUNCTION PAIRS 25
3.7 REFERENCES 28

4 HIGH-FREQUENCY REFRACTIVE INDEX TENSOR **30**

4.1 HIGH-FREQUENCY REFRACTIVE INDEX 30
4.2 FORMULATION OF UNIT-CELL POLARIZABILITY 30
4.3 CONSTRUCTION OF THE REFRACTIVE INDEX TENSOR 33
4.4 REFRACTIVE INDEX TENSOR FOR A *N*-HEXATRIACONTANE CRYSTAL 34
4.5 REFERENCE 42

5 4×4 TRANSFER MATRIX METHOD 44

5.1 BACKGROUND OF 4×4 TRANSFER MATRIX METHOD 44
5.2 IMPLEMENTATION OF 4×4 TRANSFER MATRIX METHOD 46
5.3 FRESNEL'S EQUATIONS: REFLECTION AND TRANSMISSION FOR 3-LAYER ISOTROPIC MEDIA 59
5.4 TESTING OF 4×4 TRANSFER MATRIX FOR THE ISOTROPIC CASE 60
5.5 REFERENCES 67

6 INFRARED REFLECTION ABSORPTION SPECTROSCOPY (IRRAS) SIMULATEDFROM MOLECULAR DYNAMICS (MD) MODELS 69

6.1 BASIC THEORY OF IRRAS 69
6.2 QUANTITATIVE ANALYSIS OF SPECTROSCOPIC INTENSITIES 70
6.3 TESTING 71
6.4 REFERENCE 78

7 CONCLUSION 79

7.1 REFERENCES 81

Chapter 1

Introduction

Molecular monolayers are of great interest for a very long time due to their enormous success in a wide variety of applications in nanotechnology, organic electrons, lithography, surface coating for prevention of corrosion, chemical sensing and many other applications.[1-11] Among the most important are the self-assembled monolayers (SAMs), ordered monolayers which form by the adsorption and self-assembly of surfactant molecules on solid surfaces. This field of SAMs has been of great interest for over 35 years because they form easily and are chemically stable. They are used as model systems for studying fundamental phenomena of physical chemistry and statistical physics. Since then, many SAM systems have been investigated for their potential applications in science and technology. Surprisingly, the details of these structures have been yet to be established. Many methods have been used to characterization their structure, order, and interfacial properties. Infrared spectroscopy (IRS) has proven to be a very powerful tool to measure the molecular orientation and the other structural aspects of SAMs experimentally. But to fully harness the information about their unique feature, the spectra need to be compared to structural models. This has encouraged us to study and establish a full anisotropic optical model of the SAMs to simulate infrared reflection absorption spectroscopy (IRRAS) spectrum from molecular dynamics (MD) models and compare them with experimental measurements.

1.1 Motivation

This project is motivated by the need to compare structures produced by MD simulation with experimental measurements. We develop a method to bridge this gap using the internal structure of the monolayer for the comparison. That region is the most sensitive probe of SAM structure, which also determines the physical and chemical properties of their surface. In order to fully utilize the wide range of potential applications of the ordered monolayers like SAMs, we need to understand the relationship between the properties of the SAMs and their underlying structure. Although SAMs have been studied for decades, the details of their structure are still in dispute.

Many different surface science techniques have been employed to study the structure of SAMs. The most widely used characterization tools such as AFM[12] and STM[13, 14] are particularly useful to determine the arrangement of the surface molecular structure by real-space imaging. A wide variety of additional techniques have been used to characterize SAMs, He atom[15, 16] and X-ray diffraction,[15, 17] electrochemistry,[18-20] X-ray reflectivity,[21, 22] X-ray photoelectron spectroscopy,[23-25] wetting,[26-28] and infrared spectroscopy (IRS).[29-35] Of these, only infrared reflection absorption spectroscopy (IRRAS) probes the internal molecular structure of the SAM and the key order parameters—alkyl chain tilt and twist. Our approach is to simulate IRRAS spectra based on the molecular conformations from MD simulations, which can be compared with the experimental spectra.

1.2 Overview of Infrared Reflection Absorption Spectroscopy (IRRAS)

IRRAS is a powerful spectroscopic technique used to study ordered monolayers and thin films. It can be broadly applied to supported films on transparent and metallic substrates and can be performed *in situ* in gas and liquid environments. Due to the electromagnetic boundary conditions, IRRAS not only provides the typical chemical and structural information, but also probes the molecular orientation within the film. This method is particularly suitable for the investigation of SAMs on noble metal surfaces such as gold. The reflectance spectrum contains the conventional adsorption spectrum but is complicated by the modulation of the reflectivity from the refractive index dispersion due to the absorption. The reflection is generally conducted near grazing incidence in order to achieve maximum sensitivity. Although, this spectroscopic method is primarily used for the characterization of organic films, it is also suitable for the analysis of inorganic structures as well. We will briefly discuss the published works which have treated the samples with specific constraints and are relevant to our project.

Yen and Wong[34] presented a study of isotropic polymer thin films on semi-infinite metallic, non-metallic, and dielectric substrates. The reflectance spectra were modeled in terms of transverse optical (TO) and longitudinal optical (LO) modes, which were obtained from transmission IR experiments on the bulk phase of material. Based on the work by Berreman on

vibrational spectra on thin films, Yen and Wong recognized that while transmission IR experiments allow excitation of localized and delocalized TO modes, LO modes can also be excited in reflection at oblique incidence, particularly with *p*-polarized (TM) light for thin films adsorbed on a metallic substrate. Although their treatment was not in good agreement with the experiment, their approach to the fundamental physics was sound.[26]

Another study by Chollet *et al.* were among the first to compare the quantitative relationship between IR reflection spectra of uniaxially oriented monolayers on isotropic metallic substrates and the transmission spectra at different incident angles on transparent substrates.[35] In their treatment, the real part of the complex dielectric constants were assumed to be isotropic and constant. They used a 3-layer optical model (air-film-substrate ↔ isotropic-uniaxial-isotropic). Although, their treatment was particularly focused on oriented layers of stearamide on aluminium oxide, the treatment is not easily adapted for general applications. Ishino *et al.* reported a quantitative method to determine the reflection spectra of thin films of oriented organic polymer on non-metallic substrates.[36] Their method is applicable specifically to uniaxially oriented thin films. Their treatment cannot be extended to biaxial films.

Based on the formalism by Greenler[37] and Hansen,[38] Allara *et al.* demonstrated a general procedure for modeling isotropic thin films for IRRAS.[31, 32, 39] The dispersion relation of the real refractive index was explicitly treated in this study. They established that the dispersion of the real refractive index influences the spectral line shapes. Including this effect, they improved the model and interpretation of the spectra.[31] Isotropic thin films were considered on both metallic[31] and non-metallic[32, 39, 40] substrates. They calculated the orientation of the IR active modes of the adsorbate molecular groups from the reflection spectra by employing the anisotropy of the surface electric field. They noted that the complex refractive index should be formulated as tensor instead of a scalar to avoid the smaller changes that could occur in the surface fields. In follow up work, Parikh and Allara developed a quantitative simulation technique for uniaxial anisotropic multilayered thin films.[33] In their study, the samples consisted of small SAM domains with random azimuthal orientation, which were modeled as a uniaxial film.[33] We base our work on their approach and extend it to the full anisotropic (biaxial) treatment, therefore a briefly outline of their method is appropriate.

Modeling the IRRAS spectrum of a SAM begins with a conventional MIR spectrum of a reference phase, a randomly oriented polycrystalline sample with a structure and composition

closely related to the SAM of interest. The absorption spectrum is scaled to yield the frequency-dependent imaginary-part of the refractive index (absorption coefficient) and then deconvolved into its individual modes. Each mode has a direction (anisotropy) defined by the mode. This information is used to construct the frequency dependent complex refractive index tensor based upon a guess of the molecular orientations within the SAM. The real part of the refractive index is obtained from the imaginary part of the refractive index using the Kramers-Kronig relation. The IRRAS spectrum is obtained using the 4×4 transfer matrix optical model to calculate the reflectance spectrum, which is compared to the experimental spectrum. The molecular orientation is then adjusted and the process is repeated until the model and the experimental IRRAS spectra agree.

We adapt this strategy of comparing the IRRAS spectrum of possible structural models with the experimental spectrum. The detailed molecular structure is derived from all-atom MD simulations. An IRRAS spectrum can be calculated from these molecular structures following the strategies developed by Parikh and Allara[33] and then compared to experimental measurements. Instead of adjusting the molecular geometry to match the experimental spectra, we have modeled the IRRAS spectra from MD simulations. The models that best agree with the experimental spectra will be deemed to be the best candidates for the experimentally observed SAM structure. The reference phase must be chosen carefully because the details of the relative mode intensities, spectral widths, and Fermi resonances can be quite sensitive to inter and intramolecular interactions. Features like the IR mode frequency, absorption strength or broadening are characteristics which are imported from the reference phase. Adding these effects to the model is well beyond the scope of this project.

1.3 Overview of the Project

Our goal is to develop a full anisotropic optical model of the SAM to simulate the IRRAS spectrum based on the methods developed by Parikh and Allara.[33] In order to treat the full anisotropy of the structure, we will extend the calculation of complex refractive index by establishing a technique to calculate the high frequency refractive index tensor. The high frequency part of the refractive index tensor is calculated using the atomic bond vectors and their bond polarizabilities. The high frequency refractive index tensor is a direct summation of the bond polarizabilities in the simulated SAM. The complex refractive index tensor in the mid infrared (MIR) is calculated for the C-H stretching modes using the CH_2 and CH_3 group orientations in the simulations and the experimental data from the reference phase. In order to obtain the real part of the optical tensor, the Kramers-Kronig relation is employed to calculate the frequency dependent refractive index tensor in the MIR from the absorption of each mode. We construct the anisotropic MIR complex refractive index tensor function for the SAM based on the IR spectra of a reference phase, the bond vectors and orientations of the C-H stretching mode in the MD simulations. The 4×4 transfer matrix method is used to calculate the IRRAS spectrum in the C-H stretching region of the simulated SAM.

The present study is organized as follows. In chapter 2, a method to construct the complex refractive index tensor in the MIR from the bond polarizability and the absorption from the IR active modes is presented. The Kramers-Kronig (K-K) transformation relation is also introduced with a discussion of the three frequency regimes. In chapter 3, a brief overview of the numerical K-K transformation relations is provided. Because the spectrum can be decomposed into Gaussian and Lorentzian line shapes, we develop and verify conjugate analytic functions of these absorption line shapes for the refractive index dispersion (Kramers-Kronig transformation pairs). In chapter 4, formulation of the high-frequency refractive index tensors in terms of atomic polarizabilities and bond polarizability tensors is presented. An example of utilizing this method to calculate the high-frequency refractive index tensor for a known material is also provided. In chapter 5, the background and the implementation of the 4×4 transfer matrix method with the verification of special cases are discussed. In chapter 6, we bring all these parts together to demonstrate the simulation of IRRAS spectra from an MD model and comparison to the

experimental spectrum. In chapter 7, a summary of all our findings and the future direction of this project are discussed.

1.4 Reference

1. Nuzzo, R. G.; Allara, D. L., Adsorption of bifunctional organic disulfides on gold surfaces. *J. Am. Chem. Soc.* **1983,** *105* (13), 4481-4483.
2. Casalini, S.; Bortolotti, C. A.; Leonardi, F.; Biscarini, F., Self-assembled monolayers in organic electronics. *Chem. Soc. Rev.* **2017,** *46* (1), 40-71.
3. Love, J. C.; Estroff, L. A.; Kriebel, J. K.; Nuzzo, R. G.; Whitesides, G. M., Self-Assembled Monolayers of Thiolates on Metals as a Form of Nanotechnology. *Chem. Rev.* **2005,** *105* (4), 1103-1170.
4. Tarlov, M. J.; Burgess, D. R. F.; Gillen, G., UV photopatterning of alkanethiolate monolayers self-assembled on gold and silver. *J. Am. Chem. Soc.* **1993,** *115* (12), 5305-5306.
5. Hartwich, J.; Dreeskornfeld, L.; Heisig, V.; Rahn, S.; Wehmeyer, O.; Kleineberg, U.; Heinzmann, U., STM writing of artificial nanostructures in ultrathin PMMA and SAM resists and subsequent pattern transfer in a Mo/Si multilayer by reactive ion etching. *Appl Phys A* **1998,** *66* (1), S685-S688.
6. Magnussen, O. M.; Vogt, M. R.; Scherer, J.; Behm, R. J., Double-layer structure, corrosion and corrosion inhibition of copper in aqueous solution. *Appl Phys A* **1998,** *66* (1), S447-S451.
7. Okabe, Y.; Furugori, M.; Tani, Y.; Akiba, U.; Fujihira, M., Chemical force microscopy of microcontact-printed self-assembled monolayers by pulsed-force-mode atomic force microscopy. *Ultramicroscopy* **2000,** *82* (1), 203-212.
8. Schilardi, P. L.; Azzaroni, O.; Salvarezza, R. C., A Novel Application of Alkanethiol Self-Assembled Monolayers in Nanofabrication: Direct Molding and Replication of Patterned Conducting Masters. *Langmuir* **2001,** *17* (9), 2748-2752.
9. Klutse, C. K.; Mayer, A.; Wittkamper, J.; Cullum, B. M., Applications of Self-Assembled Monolayers in Surface-Enhanced Raman Scattering. *J. Nanotechnol.* **2012,** *2012*, 319038.
10. Gooding, J. J.; Hibbert, D. B., The application of alkanethiol self-assembled monolayers to enzyme electrodes. *Trac-Trend Anal Chem* **1999,** *18* (8), 525-533.
11. Celestin, M.; Krishnan, S.; Bhansali, S.; Stefanakos, E.; Goswami, D., A review of self-assembled monolayers as potential terahertz frequency tunnel diodes. *Nano Res.* **2014,** *7* (5), 589-625.
12. Schreiber, F., Structure and growth of self-assembling monolayers. *Prog. Surf. Sci.* **2000,** *65* (5), 151-257.
13. Dhirani, A.-A.; Zehner, R. W.; Hsung, R. P.; Guyot-Sionnest, P.; Sita, L. R., Self-Assembly of Conjugated Molecular Rods: A High-Resolution STM Study. *J. Am. Chem. Soc.* **1996,** *118* (13), 3319-3320.
14. Torrelles, X.; Pensa, E.; Cortés, E.; Salvarezza, R.; Carro, P.; Hernández Guerrero, C.; Ocal, C.; Barrena, E.; Ferrer, S., Solving the Long-Standing Controversy of Long-Chain Alkanethiols Surface Structure on Au(111). *J. Phys. Chem. C* **2018,** *122* (7), 3893-3902.
15. III, N. C.; Chidsey, C. E. D.; Eisenberger, P.; Fenter, P.; Li, J.; Liang, K. S.; Liu, G. Y.; Scoles, G., Structural defects in self‐assembled organic monolayers via combined atomic beam and x‐ray diffraction. *J. Phys. Chem. A* **1993,** *99* (1), 744-747.

16. Camillone, N.; Leung, T. Y. B.; Schwartz, P.; Eisenberger, P.; Scoles, G., Chain Length Dependence of the Striped Phases of Alkanethiol Monolayers Self-Assembled on Au(111): An Atomic Beam Diffraction Study. *Langmuir* **1996,** *12* (11), 2737-2746.
17. Fenter, P.; Eberhardt, A.; Eisenberger, P., Self-Assembly of n-Alkyl Thiols as Disulfides on Au(111). *Science* **1994,** *266* (5188), 1216-1218.
18. Dijksma, M.; Kamp, B.; Hoogvliet, J. C.; van Bennekom, W. P., Formation and Electrochemical Characterization of Self-Assembled Monolayers of Thioctic Acid on Polycrystalline Gold Electrodes in Phosphate Buffer pH 7.4. *Langmuir* **2000,** *16* (8), 3852-3857.
19. Hillebrandt, H.; Tanaka, M., Electrochemical Characterization of Self-Assembled Alkylsiloxane Monolayers on Indium−Tin Oxide (ITO) Semiconductor Electrodes. *J. Phys. Chem. B* **2001,** *105* (19), 4270-4276.
20. Sabapathy, R. C.; Bhattacharyya, S.; Leavy, M. C.; Cleland, W. E.; Hussey, C. L., Electrochemical and Spectroscopic Characterization of Self-Assembled Monolayers of Ferrocenylalkyl Compounds with Amide Linkages. *Langmuir* **1998,** *14* (1), 124-136.
21. Sheller, N. B.; Petrash, S.; Foster, M. D.; Tsukruk, V. V., Atomic Force Microscopy and X-ray Reflectivity Studies of Albumin Adsorbed onto Self-Assembled Monolayers of Hexadecyltrichlorosilane. *Langmuir* **1998,** *14* (16), 4535-4544.
22. Evans, S. D.; Goppert-Berarducci, K. E.; Urankar, E.; Gerenser, L. J.; Ulman, A.; Snyder, R. G., Monolayers having large in-plane dipole moments: characterization of sulfone-containing self-assembled monolayers of alkanethiols on gold by Fourier transform infrared spectroscopy, x-ray photoelectron spectroscopy and wetting. *Langmuir* **1991,** *7* (11), 2700-2709.
23. Fenter, P.; Eberhardt, A.; Eisenberger, P., Self-Assembly of n-Alkyl Thiols as Disulfides on Au(111). *Science* **1994,** *266* (5188), 1216.
24. Heister, K.; Allara, D. L.; Bahnck, K.; Frey, S.; Zharnikov, M.; Grunze, M., Deviations from 1 : 1 compositions in self-assembled monolayers formed from adsorption of asymmetric dialkyl disulfides on gold. *Langmuir* **1999,** *15* (17), 5440-5443.
25. Fisher, G. L.; Hooper, A.; Opila, R. L.; Jung, D. R.; Allara, D. L.; Winograd, N., The interaction between vapor-deposited Al atoms and methylester-terminated self-assembled monolayers studied by time-of-flight secondary ion mass spectrometry, X-ray photoelectron spectroscopy and infrared reflectance spectroscopy. *J. Electron Spectros. Relat. Phenomena* **1999,** *98-99*, 139-148.
26. Laibinis, P. E.; Whitesides, G. M.; Allara, D. L.; Tao, Y. T.; Parikh, A. N.; Nuzzo, R. G., Comparison of the structures and wetting properties of self-assembled monolayers of n-alkanethiols on the coinage metal surfaces, copper, silver, and gold. *J. Am. Chem. Soc.* **1991,** *113* (19), 7152-7167.
27. Dubois, L. H.; Nuzzo, R. G., Synthesis, Structure, and Properties of Model Organic Surfaces. *Annu. Rev. Phys. Chem.* **1992,** *43* (1), 437-463.
28. Nuzzo, R. G.; Dubois, L. H.; Allara, D. L., Fundamental studies of microscopic wetting on organic surfaces. 1. Formation and structural characterization of a self-consistent series of polyfunctional organic monolayers. *J. Am. Chem. Soc.* **1990,** *112* (2), 558-569.
29. Bensebaa, F.; Ellis, T. H.; Badia, A.; Lennox, R. B., Thermal Treatment of n-Alkanethiolate Monolayers on Gold, As Observed by Infrared Spectroscopy. *Langmuir* **1998,** *14* (9), 2361-2367.
30. Porter, M. D.; Bright, T. B.; Allara, D. L.; Chidsey, C. E. D., Spontaneously organized molecular assemblies. 4. Structural characterization of n-alkyl thiol monolayers on gold by optical

ellipsometry, infrared spectroscopy, and electrochemistry. *J. Am. Chem. Soc.* **1987,** *109* (12), 3559-3568.
31. Allara, D. L.; Baca, A.; Pryde, C. A., Distortions of Band Shapes in External Reflection Infrared Spectra of Thin Polymer Films on Metal Substrates. *Macromolecules* **1978,** *11* (6), 1215-1220.
32. Allara, D. L.; Nuzzo, R. G., Spontaneously organized molecular assemblies. 2. Quantitative infrared spectroscopic determination of equilibrium structures of solution-adsorbed n-alkanoic acids on an oxidized aluminum surface. *Langmuir* **1985,** *1* (1), 52-66.
33. Parikh, A. N.; Allara, D. L., Quantitative determination of molecular structure in multilayered thin films of biaxial and lower symmetry from photon spectroscopies. I. Reflection infrared vibrational spectroscopy. *J. Chem. Phys.* **1992,** *96* (2), 927-945.
34. Yen, Y. S.; Wong, J. S., Infrared reflectance properties of surface thin films. *Am. J. Phys. Chem.* **1989,** *93* (20), 7208-7216.
35. Chollet, P. A.; Messier, J.; Rosilio, C., Infrared determination of the orientation of molecules in stearamide monolayers. *J. Chem. Phys.* **1976,** *64* (3), 1042-1050.
36. Ishino, Y.; Ishida, H., Spectral simulation of uniaxially oriented monolayers in the infrared. *Langmuir* **1988,** *4* (6), 1341-1346.
37. Greenler, R. G., Infrared Study of Adsorbed Molecules on Metal Surfaces by Reflection Techniques. *J. Chem. Phys.* **1966,** *44* (1), 310-315.
38. Hansen, W. N., A New Spectrophotometric Technique Using Multiple Attenuated Total Reflection. *Anal. Chem.* **1963,** *35* (6), 765-766.
39. Allara, D. L.; Nuzzo, R. G., Spontaneously organized molecular assemblies. 1. Formation, dynamics, and physical properties of n-alkanoic acids adsorbed from solution on an oxidized aluminum surface. *Langmuir* **1985,** *1* (1), 45-52.
40. Porter, M. D.; Bright, T. B.; Allara, D. L.; Kuwana, T., Quantitative aspects of infrared external reflection spectroscopy: polymer/glassy carbon interface. *Anal. Chem.* **1986,** *58* (12), 2461-2465.

Chapter 2

Construction of the Complex Refractive Index Tensor

Optical properties such as refractive index of a given crystal is dependent on the direction of propagation of the wave as well as the polarization of the incident light. In an isotropic material, polarization is induced by the electric field of the incident wave and the direction of the polarization is parallel to the applied field. But in an anisotropic crystal, the induced dipoles are not necessarily aligned with the electric field. The phase velocity of the light wave in the anisotropic medium is dependent on the state and the direction of the polarization. Generally, for any given direction of propagation, there exist two waves, with orthogonal polarization directions determined by the crystal axes. Therefore, the anisotropic refractive index demands a more complex treatment than isotropic medium. A complex refractive index must be introduced in order to describe the full anisotropy of a given crystal. The index of refraction of a material depends on the symmetry of the structure as well. Evaluation of the complex refractive index tensor of an unknown crystal will provide us an insight on the geometry and the molecular conformation of the unknown compound as well as the symmetry of the crystal. In our study, we are going to model the refractive index of n-alkanethiol self-assembled monolayers (SAMs) in the mid-IR region and will calculate the complex refractive index tensor in order to identify the structural properties of SAMs. Optical spectroscopy such as infrared reflection absorption spectra (IRRAS) measures the refractive index from the reflection absorption spectra from the surface of sample. The measured spectra in the mid-IR region are function of polarization and angle of incidence. Hence, the dielectric permittivity constant can be derived directly from the index of refraction. In the following sections, we present a discussion on how the complex refractive index tensor of an anisotropic medium can be constructed from the bond polarizability of a molecule and absorption from the IR active modes in the mid-IR region.

2.1 Complex Refractive Index Tensor

In this section we discuss the underlying physics behind the refractive index, specifically the relationship between the refractive index and optical absorption. In a dielectric medium, the

ratio of the speed of light in vacuum, c, to its phase velocity in the medium, v_p, is known as the refractive index, n

$$n = \frac{c}{v_p} \ . \tag{2.1}$$

Both the speed of light and the phase velocity are related to the (electric) permittivity and (magnetic) permeability in vacuum and the specific medium, respectively. The relationship is

$$c = \frac{1}{\sqrt{\varepsilon_0 \mu_0}} \quad \text{and} \quad v_p = \frac{1}{\sqrt{\varepsilon \mu}} \ , \tag{2.2}$$

where, ε_0 and ε are the permittivity in vacuum and in a medium and μ_0 and μ are the permeability constants in vacuum and in the medium, respectively. From eq. (2.2) and eq. (2.1), n can be expressed in terms of relative permittivity, ε_r, and relative permeability, μ_r,

$$n = \sqrt{\frac{\varepsilon}{\varepsilon_0}\frac{\mu}{\mu_0}} = \sqrt{\varepsilon_r \mu_r} \ . \tag{2.3}$$

In our study, we assume the medium is nonmagnetic, therefore, $\mu_r = 1$ and eq. (2.3) becomes simply $n = \sqrt{\varepsilon_r}$. This is a fundamental relationship between the optical property, refractive index, and the material property, relative permittivity, ε_r. The polarization of a material in response to an applied electric field is expressed by the permittivity. The greater the polarization of a material for a given applied electric field, the greater ε_r will be. Both the relative permittivity and refractive index of a wave are dependent upon the frequency of that wave. If the medium is lossy (one that absorbs energy from the wave), the wave propagating through this medium will be attenuated by absorption. Lossy materials are generally characterized by a frequency dependent complex relative permittivity.

$$\varepsilon(\omega) = \varepsilon_1(\omega) + i\varepsilon_2(\omega) \tag{2.4}$$

Here and in the remaining discussion, we drop the "*r*" subscript and adopt the more conventional term for the relative permittivity, the dielectric constant, ε, where ω is the angular frequency and ε_1 and ε_2 are the real and imaginary parts. The corresponding complex refractive index, $\tilde{n}$, is defined[1]

$$\tilde{n}(\omega) = n(\omega) + i\kappa(\omega) \tag{2.5}$$

where the real part and imaginary parts of $\tilde{n}(\omega)$ are denoted by $n(\omega)$ and $\kappa(\omega)$, respectively. The real part, n is defined in eq. (2.1). The imaginary part, κ describes the rate of attenuation of the wave in that medium. The response of the material is described by ε, while the wave propagation through the medium is described by $\tilde{n}$. We can write the relationship between both these complex quantities

$$\begin{aligned} \varepsilon &= \tilde{n}^2 \\ \varepsilon_1 + i\varepsilon_2 &= \left(n + i\kappa\right)^2 \end{aligned} \tag{2.6}$$

and between their components

$$\begin{aligned} &\varepsilon_1 = n^2 - \kappa^2 \; ; \quad \varepsilon_2 = 2n\kappa \; ; \\ &n = \sqrt{\tfrac{1}{2}\left(|\varepsilon| + \varepsilon_1\right)} \; ; \quad \kappa = \sqrt{\tfrac{1}{2}\left(|\varepsilon| - \varepsilon_1\right)} \; ; \quad |\varepsilon| = \sqrt{\varepsilon_1^2 + \varepsilon_2^2} \; . \end{aligned} \tag{2.7}$$

We need to make an important distinction between absorption, the loss of energy to the medium, which is described by ε_2, and the attenuation of the wave, which is described by κ. The most common example, of wave attenuation with very little energy loss to the medium is wave propagation in the good metal ($\varepsilon_1 < 0$ and $\varepsilon_2 < -\varepsilon_1$). The wave is strongly attenuated upon entering the metal (large κ). The negative ε_1 describes the response of the metal which generates an internal electric field opposing that of the incident wave. The result is conversion of the incident wave energy into the reflected wave energy, resulting in strong attenuation without absorption. In typical molecular systems, as in our studies ($\varepsilon_1 > 0$ and $\varepsilon_2 < \varepsilon_1$), attenuation is caused by absorption, thus the distinction is not needed as it is in metals.

2.1.1 Electromagnetic Wave Propagation and Absorption

Electromagnetic phenomena (e.g. reflection, refraction, transmission, and absorption) are described by Maxwell's equations.[2] For an electromagnetic plane wave propagating in the positive z-direction through a homogeneous and optically isotropic medium, the strength of the oscillating electric field can be written as[2]

$$E = E_0 \exp\left(ikz - i\omega t\right), \tag{2.8}$$

where k is the wave vector. When the wave is travelling through a medium of refractive index $\tilde{n}$, the relationship between the wave vector, k and the angular frequency, ω, is given by

$$k = \tilde{n}\frac{\omega}{c} = \tilde{n}k_0 \ , \tag{2.9}$$

where, k_0 is the vacuum wave vector. In media with a complex refractive index eq. (2.9) becomes

$$k = \left(n + i\kappa\right)k_0 \ . \tag{2.10}$$

The imaginary part of $\tilde{n}$ introduces a real term into argument of the exponential

$$E = E_0 \exp\left(i\left(n + i\kappa\right)k_0 z - i\omega t\right) = E_0 \exp\left(-\kappa k_0 z\right)\exp\left(ink_0 z - i\omega t\right). \tag{2.11}$$

The wave amplitude is attenuated exponentially with distance described by the factor, $\exp\left(-\kappa k_0 z\right)$. We can connect this result to the Beer-Lambert law which describes how the intensity of a wave decreases with distance through an absorbing medium with a decay constant α. To compare the amplitude decay constant from eq. (2.11) we must square the amplitude to obtain intensity, thereby introducing the factor of 2 into the intensity decay constant.

$$\exp\left(-\alpha z\right) = \frac{I}{I_0} = \frac{E^2}{E_0^2} = \exp\left(-2k_0\kappa z\right) \tag{2.12}$$

Here I is the intensity of the transmitted wave in the medium after propagating a distance z, I_0 is the initial intensity of the wave. We can write the relationship between α and κ as

$$\alpha = 2k_0\kappa = \frac{4\pi}{\lambda_0}\kappa \ , \tag{2.13}$$

where, $k_0 = 2\pi/\lambda_0$ and λ_0 is the free-space wavelength of the light.

2.1.2 Refractive Index Tensor in Anisotropic Medium

In isotropic media the propagation characteristics of a plane wave are independent of the direction of the propagation and the displacement vector **D** and its associated electric field **E** are parallel to each other

$$\boldsymbol{D} = \varepsilon_0\varepsilon\boldsymbol{E} \ . \tag{2.14}$$

Here, ε_0 is the permittivity of vacuum and ε is the dielectric constant (relative permittivity). In isotropic media the dielectric constant is a scalar. In anisotropic media **D** and **E** are not parallel in

general. The relationship depends on the direction of the electric field in the medium and is described by the dielectric tensor, ε_{ij}. Eq. (2.14) becomes

$$D_i = \varepsilon_0 \varepsilon_{ij} E_j \ . \tag{2.14a}$$

In matrix form, with respect to three arbitrary orthogonal axes

$$\hat{\varepsilon} = \begin{pmatrix} \varepsilon_{xx} & \varepsilon_{xy} & \varepsilon_{xz} \\ \varepsilon_{yx} & \varepsilon_{yy} & \varepsilon_{yz} \\ \varepsilon_{zx} & \varepsilon_{zy} & \varepsilon_{zz} \end{pmatrix}, \tag{2.15}$$

Equation (2.14a) can be rewritten as

$$\begin{aligned} D_x &= \varepsilon_0 (\varepsilon_{xx} E_x + \varepsilon_{xy} E_y + \varepsilon_{xz} E_z) \\ D_y &= \varepsilon_0 (\varepsilon_{yx} E_x + \varepsilon_{yy} E_y + \varepsilon_{yz} E_z) \ . \\ D_z &= \varepsilon_0 (\varepsilon_{zx} E_x + \varepsilon_{zy} E_y + \varepsilon_{zz} E_z) \end{aligned} \tag{2.16}$$

The dielectric tensor must be symmetric such that

$$\varepsilon_{ij} = \varepsilon_{ji} \ . \tag{2.17}$$

It is a general property of symmetric matrices that they can be diagonalized by a suitable choice of the coordinate axes, referred to as the principal axes of the material. The principal components along each of the axes, x, y, and z, are referred to as ε'_x, ε'_y, and ε'_z, respectively. The prime, $\hat{\varepsilon}'$ denotes the tensor in diagonalized reference frame.

$$\begin{pmatrix} D_x \\ D_y \\ D_z \end{pmatrix} = \varepsilon_0 \begin{pmatrix} \varepsilon'_x & 0 & 0 \\ 0 & \varepsilon'_y & 0 \\ 0 & 0 & \varepsilon'_z \end{pmatrix} \begin{pmatrix} E_x \\ E_y \\ E_z \end{pmatrix} \tag{2.18}$$

The refractive index of an anisotropic medium is also a tensor. The relationship of $\hat{\varepsilon}$ and $\hat{\tilde{n}}$ can only be established between the diagonalized tensors. This implies that $\hat{\varepsilon}'$ and $\hat{\tilde{n}}'$ have the same principal axes. The principal components of the refractive index are then $\tilde{n}'_x$, $\tilde{n}'_y$ and $\tilde{n}'_z$. The tensorial form of the refractive index becomes

$$\hat{\tilde{n}}' = \begin{pmatrix} \tilde{n}'_x & 0 & 0 \\ 0 & \tilde{n}'_y & 0 \\ 0 & 0 & \tilde{n}'_z \end{pmatrix}. \tag{2.19}$$

This relationship extends to the complex dielectric constant and the complex refractive index such that

$$\varepsilon_i = \tilde{n}_i^2 \ , \tag{2.19a}$$

which holds independently for each of the principal axes. Transforming between $\hat{\varepsilon}$ and $\hat{\tilde{n}}$ can only be done with the diagonalized tensor. Therefore, starting from a tensor in an arbitrary non-diagonal coordinate frame requires rotation into the principal coordinate frame for transforming between $\hat{\varepsilon}'$ and $\hat{\tilde{n}}'$ followed by rotating the result back into the original coordinate frame.

2.2 The Kramers-Kronig Relation

The fundamental principal of physics which states that a material cannot respond before it is acted upon is known as the principal of causality. When causality is applied to linear optical spectroscopy, significant properties of symmetry and relationships are produced. These relationships are very useful in modeling and analyzing different optical properties. As a result of these symmetry properties, the real and imaginary part of complex refractive index i.e., n and κ are related by the Kramers-Kronig relationship. They can be described as Kramers-Kronig transformations pairs. In the following sections, a discussion of the Kramers-Kronig relationship and how it is employed to calculate the total complex refractive index tensor are presented.

2.2.1 Calculation of Refractive Index from the Absorption Spectrum

The K-K transformation relations are widely used in calculating the refractive index directly from the frequency dependent absorption in linear and non-linear optics. The transformation requires that the frequency dependence of κ be known over a frequency range as wide as possible. We can then use K-K relations to find $n(\omega)$ from $\kappa(\omega)$[3-5]

$$n(\omega_0) = \frac{2}{\pi} \mathcal{P} \int_0^\infty \frac{\kappa(\omega')\omega' d\omega'}{\omega'^2 - \omega_0^2} \ , \tag{2.20}$$

where ω' is the integration variable. Here, $\mathcal{P}$ indicates the Cauchy principal value of the integral and the singularity has been avoided at $\omega' = \omega_o$. Experimentally we cannot measure the

absorption spectrum from DC to infinite frequency, however we can make some useful approximations. We divide the frequency range into three separate regimes and rewrite the expression (2.20) as

$$n(\omega_0) = \frac{2}{\pi}\mathcal{P}\left(\int_0^{\omega_a} \frac{\kappa(\omega')\omega' d\omega'}{\omega'^2 - \omega_0^2} + \int_{\omega_a}^{\omega_b} \frac{\kappa(\omega')\omega' d\omega'}{\omega'^2 - \omega_0^2} + \int_{\omega_b}^{\infty} \frac{\kappa(\omega')\omega' d\omega'}{\omega'^2 - \omega_0^2} \right). \quad (2.21)$$

The range ω_a and ω_b is the region where we know $\kappa(\omega)$ and where we are explicitly interested in $n(\omega)$. The low frequency region, 0 to ω_a, can be ignored because it contributes very little to n above ω_a. The high frequency region, ω_b to ∞, contributes a constant term to n below ω_b.

2.2.2 Dielectric Dispersion and Frequency Response Regions

Dielectric constant $\varepsilon(\omega)$ is the fundamental property of a material which describes the ability to polarize a material subjected to a time-varying electric field. The real and imaginary parts describe how electromagnetic energy is stored in the material and how the energy is dissipated, respectively. Recall that the real and imaginary components of $\varepsilon(\omega)$ are related to the real and imaginary parts of complex refractive index $\tilde{n}(\omega)$, eq. (2.7). In this section we discuss the dielectric dispersion and use that as the basis to reduce the range of frequencies that need to be explicitly considered for the K-K relation.

The processes which describe the polarization response of a material to an applied electric field are frequency dependent. The origin of the material response can arise from a variety of mechanisms, e.g. electronic, atomic, and dipolar. Each contributes to the dielectric constant, but each have a characteristic time scale or resonant frequency. At time scales much shorter than the characteristic time scale (far above the resonant frequency), that mechanism contributes very little to the dielectric response. Near the resonant frequency, that mechanism contributes strongly to the dielectric response, and particularly to the imaginary part. At longer time scales (lower frequencies) the mechanism contributes to dielectric response but is insensitive to the frequency.

The three example mechanisms, electronic polarization has the shortest time scale, roughly the time it takes for an electron to move from one side of the electron cloud to the other, corresponding to the UV frequency region. In this mechanism the applied electric field causes

the negatively charged electron cloud to be displaced relative to the positively charged nucleus. Atomic polarization has an intermediate time scale corresponding to the MIR region of the spectrum. In this mechanism the applied electric field interacts with the changing in dipole moment of molecules as their atomic bonds vibrate and bend. Dipolar polarization has the longest time scale of the three examples, corresponding to time scales in the microwave region. In this mechanism the applied electric field causes dipolar molecules to rotate and orient with the field.

We are interested in the molecular vibrations in the MIR region. We can ignore the low frequency region because that will contribute very little to *n*. The high frequency region will be important but does not contribute to the frequency dependence of *n* in the MIR, thus can be treated as a constant. Therefore, the intermediate frequency region in eq. (2.20), $\Delta n(\omega)$:

$$\Delta n(\omega) = \frac{2}{\pi}\mathcal{P}\int_{\omega_a}^{\omega_b} \frac{\kappa(\omega')\omega' d\omega'}{\omega'^2 - \omega_0^{\,2}} \ . \tag{2.22}$$

Similarly, the high frequency region is the high frequency refractive index, n_∞

$$n_\infty = \frac{2}{\pi}\mathcal{P}\int_{\omega_b}^{\infty} \frac{\kappa(\omega')\omega' d\omega'}{\omega'^2 - \omega_0^{\,2}} \, . \tag{2.23}$$

We see that eq. (2.20) can be re-written as a frequency dependent component from the MIR contribution, and a high frequency (visible) constant term[6-8]

$$n(\omega) = \Delta n(\omega) + n_\infty \ . \tag{2.24}$$

In chapters 3 and 4, we describe a method to calculate n_∞ and $\Delta n(\omega)$, respectively.

2.3 References

1. Nuzzo, R. G.; Dubois, L. H.; Allara, D. L., Fundamental studies of microscopic wetting on organic surfaces. 1. Formation and structural characterization of a self-consistent series of polyfunctional organic monolayers. *J. Am. Chem. Soc.* **1990,** *112* (2), 558-569.
2. Born, M.; Wolf, E.; Bhatia, A. B., *Principles of optics electromagnetic theory of propagation, interference, and diffraction of light*. 5th ed.; Oxford, New York, Pergamon Press: Oxford, New York, 1975.
3. Kramers, H. A., La diffusion de la lumiere par les atomes. *Atti Cong. Intern. Fisica (Transactions of Volta Centenary Congress) Como* **1927,** *2*, 545-557.
4. de L. Kronig, R., On the Theory of Dispersion of X-Rays. *J. Opt. Soc. Am.* **1926,** *12* (6), 547-557.

5. Seitz, F.; Turnbull, D.; Anderson, P. W., Solid State Physics: Advances in Research and Applications. *J. Electrochem. Soc.* **1956,** *103* (8), 181C.
6. Allara, D. L.; Baca, A.; Pryde, C. A., Distortions of Band Shapes in External Reflection Infrared Spectra of Thin Polymer Films on Metal Substrates. *Macromolecules* **1978,** *11* (6), 1215-1220.
7. Allara, D. L.; Nuzzo, R. G., Spontaneously organized molecular assemblies. 2. Quantitative infrared spectroscopic determination of equilibrium structures of solution-adsorbed n-alkanoic acids on an oxidized aluminum surface. *Langmuir* **1985,** *1* (1), 52-66.
8. Parikh, A. N.; Allara, D. L., Quantitative determination of molecular structure in multilayered thin films of biaxial and lower symmetry from photon spectroscopies. I. Reflection infrared vibrational spectroscopy. *J. Chem. Phys.* **1992,** *96* (2), 927-945.

Chapter 3
Analytic Function Kramers-Kronig Transform Pairs

The aim of the work in this chapter is to develop a set of analytic function pairs for calculation of the real refractive index from a parametrized absorption spectrum. We make use of the Kramers-Kronig (K-K) relationship to provide the needed connection. This work was inspired by the common practice of fitting the peaks in an absorption spectrum to a linear combination of Gaussian-Lorentzian peak shapes. Both functions have analytic representations in $\kappa(\omega)$ and the K-K conjugate $\Delta n(\omega)$. We show that linear combinations of these functions are also K-K conjugates. In this chapter, we present a brief overview of K-K relations, approximations to the direct integration, the analytic functions, and comparison of the analytic functions to the direct integration.

3.1 General Overview of Kramers-Kronig Relation

Optical spectroscopy has been a fundamental technique to investigate materials because it is nondestructive. Absorption spectroscopy is the most common method, in which the frequency dependence of the optical absorption is measured. It has widespread application in the science, industry, and medicine. The Beer-Lambert law describes the relation between optical absorption of the material and the attenuation of the transmitted light. Our interest is to study optical absorption in monolayer films on metals where absorption spectroscopy cannot be performed in transmission mode. These measurements can be performed in reflection mode which is a common geometry for MIR spectroscopy. This technique is variously known as reflection absorption infrared spectroscopy (RAIRS) or infrared reflection absorption spectroscopy (IRRAS). Interpreting the spectrum is more complicated than in the transmission geometry because reflection is dependent on both absorption and the real part of the refractive index. However, because the real and imaginary part of the refractive index are related by the K-K relation, the absorption can be recovered from the reflection absorption spectra.

Causality is an essential principal in physics. It states that a system cannot react before the occurrence of a stimulus. Various definitions of causality are presented by Nussenzveig.[1] The

central concept of relativistic causality states that no wave can propagate faster than the speed of light in vacuum. In optical physics, the refractive index has an analytical continuity in the upper half of the complex frequency plane. Using this concept, Kramers proved that the real part of the complex refractive index of a medium can be calculated from the spectrum of absorption and this satisfies the principal of the relativistic causality.[2] Kronig established that it is a necessary and sufficient condition for a dispersion relation to exist to satisfy a strict causality.[3] Now using the established methods by Kramers and Kronig, the fundamental relation between the real and imaginary part of the frequency dependent complex linear function can be described which is referred to as the K-K transformation relations.[2, 3] Hence, if a system satisfies the conditions of causality, it will obey K-K relations. The advantage of the causality is that the general properties can be applied in such a way that it can extract maximum amount of information about the optical properties from experimentally observed spectra. A rigorous discussion establishing the relation between the real and imaginary part of the refractive index with the aid of K-K transformation is developed in the following section.

3.2 The Kramers-Kronig Integral

In this section, a detailed analysis of the construction of the refractive index from the absorption coefficient through K-K transformation relations is presented. The real and imaginary part of the refractive index function, n and κ respectively, are related through the K-K integral transformation:

$$n(\omega) = \frac{1}{\pi} \mathcal{P} \int_{-\infty}^{\infty} \frac{\kappa(\omega')}{\omega' - \omega} d\omega' \tag{3.1}$$

$$\kappa(\omega) = -\frac{1}{\pi} \mathcal{P} \int_{-\infty}^{\infty} \frac{n(\omega')}{\omega' - \omega} d\omega' \ . \tag{3.2}$$

Here, $\mathcal{P}$ indicates the Cauchy principal value of the integral which is significant because these integrals contain a singularity. All causal impulse response functions can be decomposed into the sum of an odd and even function, which are interdependent. The real part of the response function, n is an even function of frequency and κ is an odd function of frequency.[4-6]

The advantage of representing the K-K relations as in eq. (3.1) and (3.2) is that one can see immediately that the real part of the complex refractive index can be obtained from the

imaginary part and vice versa. Apart from that advantage, it can be tricky to do the numerical integration. In most causal physical systems, the response for the positive frequencies is related to the response at negative frequencies. Therefore, the K-K integral can be written in another form where the integral requires the positive frequencies only. The integral for κ can be split into two parts as

$$n(\omega) = \frac{1}{\pi}\mathcal{P}\left\{\int_{-\infty}^{0}\frac{\kappa(\omega')}{\omega'-\omega}d\omega' + \int_{0}^{\infty}\frac{\kappa(\omega')}{\omega'-\omega}d\omega'\right\} \ . \tag{3.3}$$

In the first term of eq.(3.3), a change of variables can be made i.e., $\omega = -\omega$ and by utilizing the fact that κ is an odd function, it can be written as $\kappa(-\omega) = -\kappa(\omega)$ which ultimately becomes

$$\int_{-\infty}^{0}\frac{\kappa(\omega')}{\omega'-\omega}d\omega' = \int_{0}^{\infty}\frac{\kappa(\omega')}{\omega'+\omega}d\omega' \ . \tag{3.4}$$

Applying these changes and the properties of the odd function, the integrations can be collapsed into the range of [0, +∞] and the integral from eq. (3.3) becomes

$$n(\omega) = \frac{1}{\pi}\mathcal{P}\left\{\int_{0}^{\infty}\kappa(\omega')\left[\frac{1}{\omega'+\omega}+\frac{1}{\omega'-\omega}\right]d\omega'\right\} \ . \tag{3.5}$$

Finally, rewriting all the factors and combining them together, the K-K integral becomes

$$n(\omega) = \frac{2}{\pi}\mathcal{P}\int_{0}^{\infty}\frac{\omega'\kappa(\omega')}{\omega'^{2}-\omega^{2}}d\omega' \ . \tag{3.6}$$

Analogously, the absorption coefficient can be obtained using the K-K transformations as

$$\kappa(\omega) = -\frac{2}{\pi}\mathcal{P}\int_{0}^{\infty}\frac{\omega' n(\omega')}{\omega'^{2}-\omega^{2}}d\omega' \ . \tag{3.7}$$

As discussed in chapter 2, experimental measurements of the absorption spectrum typically are only available over a finite bandwidth. Thus, for the practical purposes, eq. (3.6) can be broken into frequency regions, (see eq. (2.24)). The frequency region of interest where the frequency dependence is needed is the only region that required integration providing $\Delta n(\omega)$. The frequency region above this contributes a constant term, the high frequency refractive index n_∞. The region below does not contribute and can be ignored. The method to analyze this high frequency refractive index will be described in the next chapter.

3.3 Numerical Kramers-Kronig Integration Approximation

In order to test the analytic functions, we will need to perform the integration in order to verify the validity of the transform pairs. The numerical problem is essentially a convolution where the integral must be evaluated fully for each point where Δn_i is needed. The singularity must be avoided in the numerical integration, which creates a gap in the sum. Although that can be compensated by increasing the density of points for the sum (smaller $\Delta\omega$), this becomes computationally expensive when the wavelength range is also large. The gap from the avoided singularity is compensated by the two terms on the right of eq. (3.6).[7]

$$\Delta n_i = \frac{2}{\pi} P\int_a^b \frac{\omega_j \kappa(\omega_j)\,\mathrm{d}\omega_j}{\omega_j^2 - \omega_i^2} = \frac{2}{\pi}\Delta\omega \sum_{j\neq i} \frac{\omega_j \kappa(\omega_j)_j}{\omega_j^2 - \omega_i^2} + \frac{1}{\pi}\Delta\omega \frac{\kappa(\omega_i)}{2\omega_i} + \frac{1}{\pi}\Delta\omega \frac{\mathrm{d}}{\mathrm{d}\omega}\kappa(\omega_i) \qquad (3.8)$$

Here $\Delta\omega$ is the frequency interval in the numerical sum. Note that the effect of the right two terms become smaller as $\Delta\omega$ is decreased. These two terms make the calculation converge much faster.

3.4 Absorption Line Shape Models

In the infrared region molecules interact with light through their vibrations, the stretching and bending of the atomic bonds. More generally, these are the normal modes of the molecular vibrations. Each mode has a signature absorption frequency depending on the atoms involved and the local environment. Thus, the infrared absorption spectrum contains structural information about molecules. The frequency width of the absorption of each mode is determined by two factors. First, the minimum line width is determined by uncertainty broadening, the lifetime of the state, and imparts a Lorentzian line shape. Second, the experiment samples the absorption of a large number of molecules, each in a slightly different environment and therefore exhibiting a slightly different absorption frequency. The random distribution of absorption frequencies about the mean lead to a Gaussian peak shape. The resulting shape is the convolution of a Lorentzian with a Gaussian (Voigt function). For simplicity, experimental line shapes can be approximated by a linear combination of a Lorentzian and a Gaussian. We would like to use convenient parameters for the spectral line shape model *viz.* the center frequency, peak height,

peak area, and peak width. These lines shapes are analytic functions which have K-K transform conjugates which are also analytic functions.

The absorption is related to the width as well as the intrinsic properties of a molecule. If all molecules experience the same broadening mechanism and become indistinguishable then the observed spectrum of an ensemble consisting a collection of organized molecules is referred to have a homogeneous broadening. This broadening is described by the Lorentzian line shape and their line centers are also same. When the molecules are placed in an environment with random perturbations, in our case, the molecules in the sample are each in a slightly different environment, then the natural linewidth gets smeared out, causing inhomogeneous broadening. In inhomogeneous broadening, the oscillators have random distribution of center frequencies and are described by the Gaussian line shape. Hence, to model the absorption line shape of our experiment, we would like to convolute these two types of broadening and define a line shape which is the linear combination of a Lorentzian and a Gaussian.

The Lorentzian distribution can be written analytically[7]

$$\kappa_L(\omega) = A\left(\frac{\gamma}{2}\right)^2\left[\frac{1}{(\omega-\omega_0)^2+\left(\frac{\gamma}{2}\right)^2}-\frac{1}{(\omega+\omega_0)^2+\left(\frac{\gamma}{2}\right)^2}\right]. \tag{3.9}$$

Here, ω_o is the center frequency, γ is peak width, the full width half maxima (FWHM), and A is peak height. The K-K transformation of eq. (3.9) can be written in analytical form

$$\Delta n_L(\omega) = A\left(\frac{\gamma}{2}\right)\left[-\frac{(\omega-\omega_0)}{(\omega-\omega_0)^2+\left(\frac{\gamma}{2}\right)^2}+\frac{(\omega+\omega_0)}{(\omega+\omega_0)^2+\left(\frac{\gamma}{2}\right)^2}\right]. \tag{3.10}$$

The second terms in eqs. (3.9) and (3.10), are the negative frequency parts required to satisfy the following odd and even function symmetry, respectively, required by causality:

$$\kappa(\omega) = -\kappa(-\omega) \tag{3.11}$$

$$n(\omega) = n(-\omega) \tag{3.12}$$

The functions for κ_L and Δn_L are show in Figure 3.1.

The Gaussian broadened absorption profile,[8]

$$\kappa(\omega) = -\sqrt{\frac{\pi}{2}}\frac{\kappa}{\gamma}\exp\left(\frac{-(\omega-\omega_0)^2}{2\gamma^2}\right). \tag{3.13}$$

And, the analytic form of the refractive index is given as

$$\Delta n(\omega) = \sqrt{\frac{\pi}{2}}\frac{\kappa}{\gamma}\exp\left(\frac{-(\omega-\omega_0)^2}{2\gamma^2}\right)\mathrm{erfi}\left(\frac{\omega-\omega_0}{\sqrt{2}\gamma}\right)$$
$$\mathrm{erfi}(x) = \frac{2}{\sqrt{\pi}}\int_0^x e^{y^2}dy \tag{3.14}$$

These analytic expressions in eq. (3.14) are not proper K-K transformation pairs because they do not follow the symmetry requirements of causal function pairs.[8] However, they can be fixed by adding a second term to each equation to correct the symmetry. For convenience, from now on we are going to write the absorption coefficient, κ as k. The new analytic form of the Gaussian absorption coefficient becomes:

$$k_G(\omega) = A\left[\exp\left\{-\frac{\log 2(\omega-\omega_0)}{\frac{1}{2}\gamma}\right\}^2 - \exp\left\{-\frac{\log 2(\omega+\omega_0)}{\frac{1}{2}\gamma}\right\}^2\right]. \tag{3.15}$$

A second issue with eq. (3.14) as presented is that while the product of the Gaussian and the imaginary error function is well behaved, the latter can return very large numbers away from the center of the peak and cause numerical headaches (overflow). The numerical problems can be avoided, by rewriting the imaginary error function in terms of the Dawson function.

$$\mathrm{erfi}(x) = \frac{2}{\sqrt{\pi}}e^{x^2}\,\mathrm{Daw}(x) \tag{3.16}$$

The leading exponential term now nicely cancels the Gaussian term yielding a simpler expression. We write the modified analytic form of Δn_G for a Gaussian absorption line shape, which is an odd function of frequency as required by causality

$$\Delta n_G(\omega) = -A\left(\frac{2}{\sqrt{\pi}}\right)\left[\mathrm{Daw}\left\{\sqrt{\log 2}\left(\frac{\omega-\omega_0}{\frac{1}{2}\gamma}\right)\right\} - \mathrm{Daw}\left\{\sqrt{\log 2}\left(\frac{\omega+\omega_0}{\frac{1}{2}\gamma}\right)\right\}\right]. \tag{3.17}$$

The functions for κ_G and Δn_G are shown in Figure 3.1.

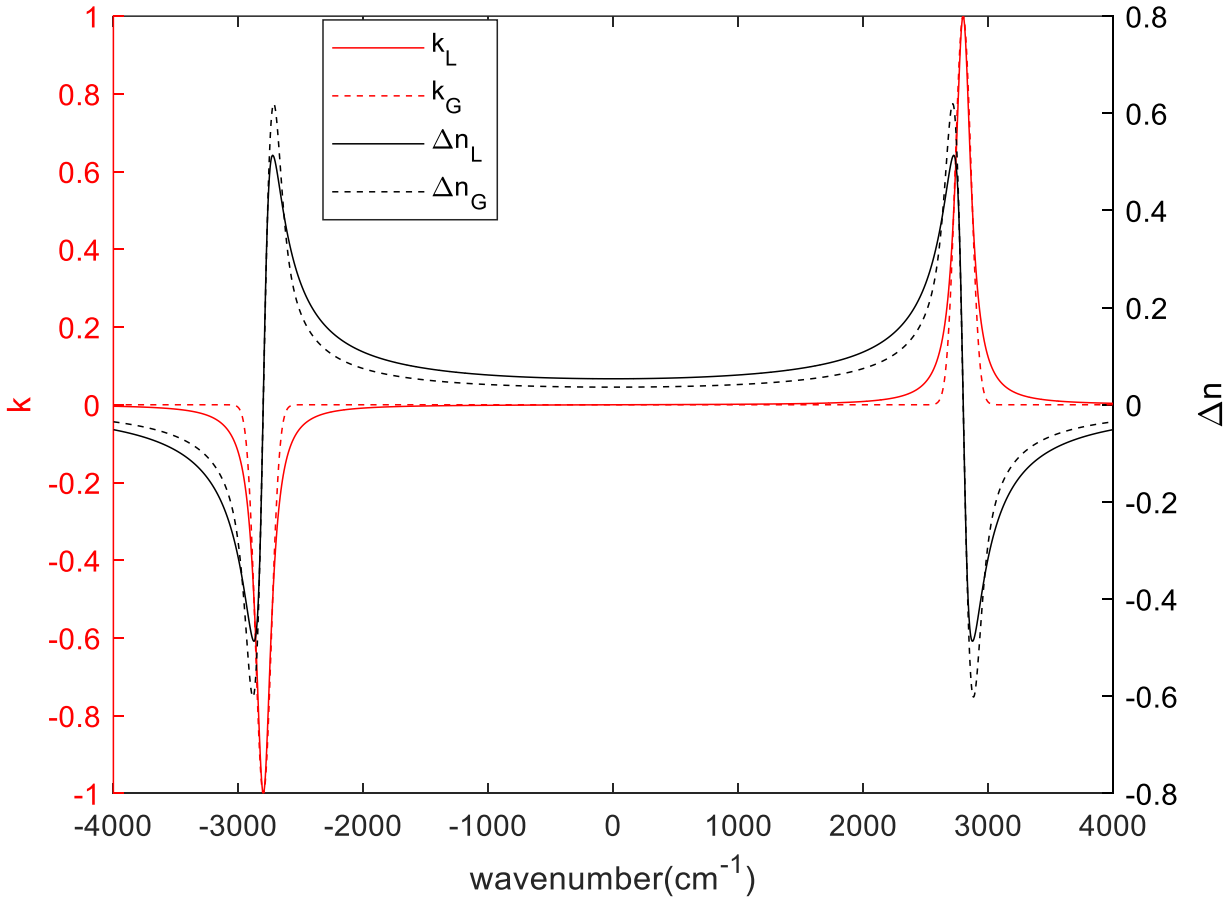

Figure 3.1: The analytic function Kramers-Kronig conjugate pairs for the Gaussian (κ_G and Δn_G) and Lorentzian (κ_L and Δn_L) line shapes. The parameters are: ω_0 = 2800 cm^{-1}; γ = 150 cm^{-1}; A = 1. Note that κ and Δn are odd function and even functions of frequency, respectively, as required by causality.

3.5 Decomposition of the Absorption Spectrum

In most condensed phase materials, infrared spectra are composed of bands whose shape can be described using Lorentzian functions, Gaussian functions, or a combination of these. Observing a pure Lorentzian or Gaussian shape is relatively rare. A more accurate representation of the absorption peak shape would be in terms of the Voigt function which is a convolution of Lorentzian with the Gaussian shape. But in practical arrangement, the Voigt function is computationally expensive. A simple linear combination of Lorentzian and Gaussian line shapes

has been found very satisfactory. In this section, we discuss the decomposition of the absorption spectrum into Lorentzian and Gaussian line shapes.

The goal of our study is to construct a linear combination of the Lorentzian and Gaussian functions which will best fit the IR absorption spectrum with variable parameters. In order to eliminate the need for numerical integration of K-K transformations, the analytic form of the absorption coefficient can be stated by combining the expressions from eqs. (3.9) and (3.15)

$$k(\omega) = A\left[Lk_L + (1-L)k_G \right] , \tag{3.18}$$

where, L defines the fraction of Lorentzian line shape which contributes to the ultimate line shape profile. For example, when L = 0, the line shape is pure Gaussian and when L = 1, the line shape will be purely Lorentzian. Similarly, we obtain the analytic form of Δn using eqs. (3.10) and (3.17) which is the conjugate K-K transformation pair of eq. (3.18)

$$\Delta n(\omega) = -A\left[L\Delta n_L + (1-L)\Delta n_G \right] . \tag{3.19}$$

In the following section, we show that these linear combinations are also a K-K conjugate pairs.

3.6 Verification of the Analytic Function Pairs

In this section we compare the analytic function pairs with the numerical evaluation of the K-K integral to verify that the linear combination of the Lorentzian and Gaussian line shapes also satisfies the K-K relation. In order to test our hypothesis, we compare Δn for a 60/40 Gaussian-Lorentzian line shape starting from the analytic for $\kappa(\omega)$, eq. (3.18). The conjugate analytic

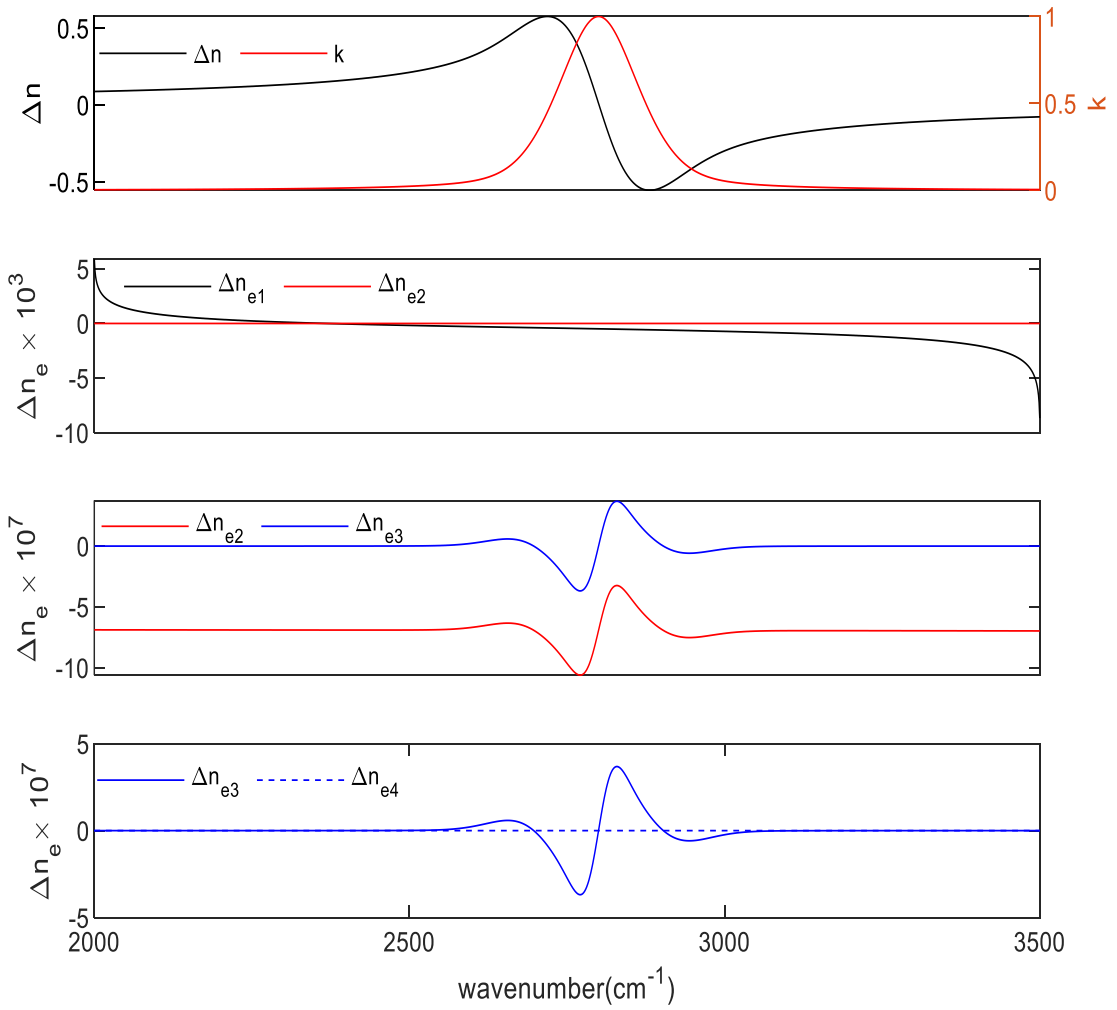

Figure 3.2: A comparison between Δn obtained from the analytic function and by numerical integration of κ for a 60/40 Gaussian-Lorentzian line shape. The parameters are: ω_0 = 2800 cm^{-1}; γ = 150 cm^{-1}; A = 1; L = 0.4. A) Comparison of κ with Δn_a (analytic) and Δn_i (numerical integration, parameters as in B) showing that they are indistinguishable on this scale. B-D) The error $\Delta n_a - \Delta n_i$ for different numerical integration parameters, range, and interval. B) Comparison between Δn_{e1} = error for the range from 2000 to 3500 cm^{-1} and Δn_{e2} = error for the range 0 to 20000 cm^{-1} for $\Delta\omega$ = 1 cm^{-1}.C) Comparison between Δn_{e2} and Δn_{e3} = error for the range from 0 to 10^6 for $\Delta\omega$ = 1 cm^{-1}. D) Comparison between Δn_{e3} and Δn_{e4} = error for the range from 0 to 10^6 cm^{-1} for $\Delta\omega$ = 0.01 cm^{-1}

function for $\Delta n_a(\omega)$, eq. (3.19), is compared to the result of the numerical integration of the K-K transform, Δn_i.

We compare the results from 2000 to 3500 cm^{-1} in Figure 3.2A. For this test, the center frequency is 2800 cm^{-1}, the FWHM is 150 cm^{-1}, and the peak height is 1. Figure 3.2B the error for the range 2000 to 3500 cm^{-1} is on the order of 10^{-3} in Δn near the center but becomes dramatically larger at the ends of the range. This is an artifact due to truncation of the K-K integral.[9-11] We verify this by extending the integration over a larger range, 0 to 20000 cm^{-1} where the ends of the range smoothens out. In Figure 3.2C the increased range reduces the truncation artifacts to the order of 10^{-12} in Δn (not shown). If we also reduce the frequency interval to $\Delta\omega = 0.01$ cm^{-1} the error reduces to the double-precision floating point error of the calculation, in Figure 3.2.D. If the analytic functions were not K-K conjugate pairs, we would expect the error to converge to a non-zero value as the accuracy of the numerical integral is increased. Thus, the error we observe are simply an artifact of the numerical integration and not due to the analytic functions. We have repeated this test for $L = 0$ to 1, and verify the linear combinations are also KK-conjugate pairs.

In Figure 3.3, we compare the shapes of $n(\omega)$ and $\kappa(\omega)$ for five different linear combinations of Gaussian and Lorentzian absorption profiles.

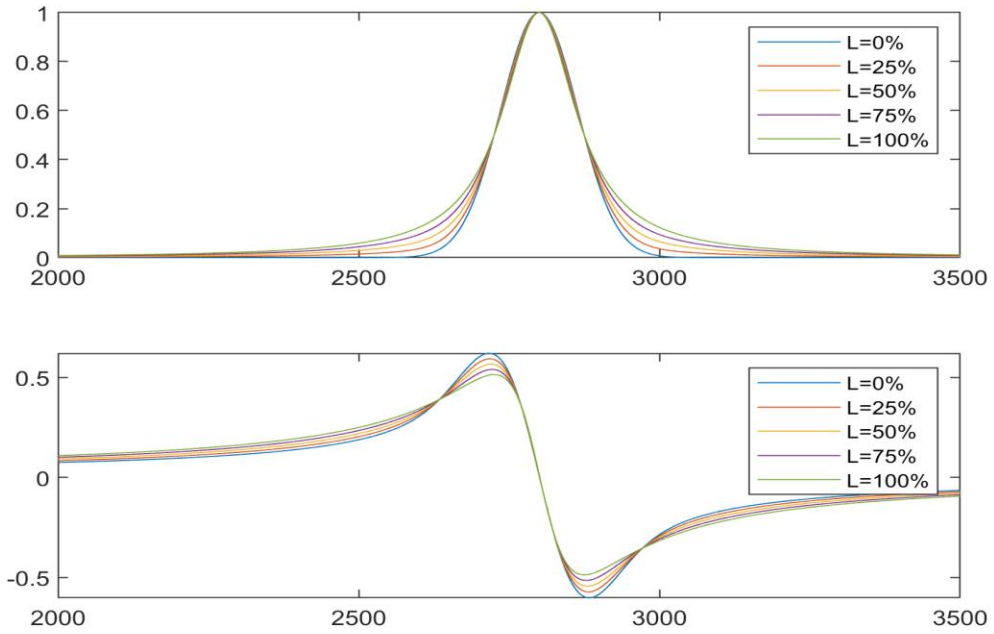

Figure 3.3: Comparison of κ and n different percentage linear combinations of Lorentzian and Gaussian absorption profiles.

In this study, we have established the analytic representation of linear combination of $n(\omega)$ and $\kappa(\omega)$ and compared it with the direct integration of K-K transformation relations. The analytic function pairs and the numerical integration of the K-K transform are in good agreement. We conclude the linear combinations are also K-K conjugate pairs. The analytic functions eliminate the computational expense and numerical artifacts of the numerical integration.

3.7 References

1. Nussenzveig, H. M., *Causality and dispersion relations / H.M. Nussenzveig*. New York : Academic Press: New York, 1972.
2. Kramers, H. A., La diffusion de la lumiere par les atomes. *Atti Cong. Intern. Fisica (Transactions of Volta Centenary Congress) Como* **1927,** *2*, 545-557.
3. de L. Kronig, R., On the Theory of Dispersion of X-Rays. *J. Opt. Soc. Am.* **1926,** *12* (6), 547-557.

4. Peterson, C. W.; Knight, B. W., Causality calculations in the time domain: An efficient alternative to the Kramers–Kronig method. *J. Opt. Soc. Am.* **1973,** *63* (10), 1238-1242.
5. Johnson, D. W., A Fourier series method for numerical Kramers-Kronig analysis. *J. Phys. A: Math. Gen* **1975,** *8* (4), 490-495.
6. Mobley, J.; Waters, K. R.; Miller, J. G., Causal determination of acoustic group velocity and frequency derivative of attenuation with finite-bandwidth Kramers-Kronig relations. *Phys. Rev. E* **2005,** *72* (1), 016604.
7. Ohta, K.; Ishida, H., Comparison Among Several Numerical Integration Methods for Kramers-Kronig Transformation. *Appl. Spectrosc.* **1988,** *42* (6), 952-957.
8. Sun, C.; Sinitsyn, N. A., Exact transition probabilities for a linear sweep through a Kramers-Kronig resonance. *J. Phys. A: Math. Theor.* **2015,** *48* (50), 505202.
9. Bowlden, H. J.; Wilmshurst, J. K., Evaluation of the One-Angle Reflection Technique for the Determination of Optical Constants. *J. Opt. Soc. Am.* **1963,** *53* (9), 1073-1078.
10. Milton, G. W.; Eyre, D. J.; Mantese, J. V., Finite Frequency Range Kramers-Kronig Relations: Bounds on the Dispersion. *Phys. Rev. Lett.* **1997,** *79* (16), 3062-3065.
11. Mobley, J.; Waters, K. R.; Hughes, M. S.; Hall, C. S.; Marsh, J. N.; Brandenburger, G. H.; Miller, J. G., Kramers–Kronig relations applied to finite bandwidth data from suspensions of encapsulated microbubbles. *J. Acoust. Soc. Am.* **2000,** *108* (5), 2091-2106.

Chapter 4

High-Frequency Refractive Index Tensor

In this chapter we develop a general method to construct the high-frequency refractive index tensor from the structure and conformation of the component molecules. The polarizability tensor for the unit cell is constructed from the bond polarizability tensors of the component molecules. We describe how the Lorentz-Lorenz equation is applied to anisotropic materials to calculate the refractive index tensor from the unit cell polarizability tensor. This method is vetted by calculating the refractive index tensor for *n*-hexatriacontane crystal and comparing our results to the experimentally measured refractive index tensor.

4.1 High-Frequency Refractive Index

The refractive index in the high-frequency region, n_∞, is sufficiently far from the absorption that it can be assumed to be real and a weak function of frequency. We can use the refractive index in the visible spectrum for n_∞ because we are interested in the frequency dependence of the refractive index in the mid infrared. The refractive index is tabulated for the widest range of substances for the sodium D line (589 nm). This is a reasonable approximation provided there are no strong absorptions in the intervening region. However, to construct a full anisotropic model requires the high frequency refractive index tensor, $\hat{n}_\infty$ which is available from the literature for a comparatively small subset of materials. In addition, the tensor is dependent not only on the substance, but also on the molecular arrangement within the crystal and, in our application, the molecular arrangement within the SAM. In the remainder of this chapter we will simply refer to $\hat{n}_\infty$ as $\hat{n}$.

4.2 Formulation of Unit-Cell Polarizability

Electromagnetic waves, with an electric field **E**, oscillating with frequency ω, propagating through a material medium induce a polarization **P** that is proportional to the electric field.

$$\mathbf{P} = \alpha \mathbf{E} \tag{4.1}$$

The proportionality constant α is defined as the polarizability of the material. In isotropic materials α is a scalar. However, many materials are optically anisotropic and therefore exhibit polarizabilities dependent on direction of **E**. For this anisotropic case, the polarizability is a second rank tensor, $\hat{\alpha}$.

$$\hat{\alpha} = \begin{bmatrix} \alpha_{xx} & \alpha_{xy} & \alpha_{xz} \\ \alpha_{yx} & \alpha_{yy} & \alpha_{yz} \\ \alpha_{zx} & \alpha_{zy} & \alpha_{zz} \end{bmatrix} \tag{4.2}$$

It is a general property of the polarizability tensor that it is a symmetric matrix and therefore can always be diagonalized by rotation into an appropriate coordinate frame. The orthogonal coordinate axes which diagonalize $\hat{\alpha}$ are termed the *principal axes*. The diagonal elements are termed the *principal values*. This is important because the relationships between polarizability, refractive index, and dielectric constant are only defined between the principal values. In our discussion we will use $\hat{\alpha}'$ to indicate the tensor in the principal coordinate frame. The principal values, α'_{xx}, α'_{yy}, and α'_{zz} can be simply written α_x, α_y and α_z.

$$\hat{\alpha}' = \begin{bmatrix} \alpha'_{xx} & 0 & 0 \\ 0 & \alpha'_{yy} & 0 \\ 0 & 0 & \alpha'_{zz} \end{bmatrix} = \begin{bmatrix} \alpha_x & 0 & 0 \\ 0 & \alpha_y & 0 \\ 0 & 0 & \alpha_z \end{bmatrix} \tag{4.3}$$

The polarizability tensor can be visualized geometrically as an ellipsoid with three orthogonal semi-axes α_x, α_y and α_z.[1] The equation for the ellipsoid is

$$\frac{x^2}{\alpha_x^2} + \frac{y^2}{\alpha_y^2} + \frac{z^2}{\alpha_z^2} = 1 \ . \tag{4.4}$$

We will make use of the additivity of polarizabilities: the polarizability of a material is the sum of the polarizabilities of its constituents. This property has been used to predict the polarizability of materials from the known polarizabilities of other materials. The polarizabilities of the constituents are deduced empirically. (In some older literature the term *refractivity* is used for *polarizability*.) The constituents can be defined as atoms, ions, etc. For organic molecules, the constituents can be chemical functional groups, CH_2, CH_3, etc., or chemical bonds, C-H, C-C, etc. The constituents also can be treated as isotropic or anisotropic entities. Obviously, the anisotropic case requires knowledge of the orientation of the constituents. In this work, we adopt the bond polarizability approach developed by Denbigh[2] where the chemical bonds are the

constituents, which is well suited for our anisotropic treatment. The polarizability of the unit cell is the sum of the polarizabilities of each bond for all the molecules within it.

$$\hat{\alpha} = \sum_i \hat{\alpha}_i \tag{4.5}$$

The summation extends over all *i* bonds. The bond polarizabilities are assumed to have cylindrical symmetry with a longitudinal component ($\alpha_{\parallel}$) along the bond axis and transverse components ($\alpha_{\perp}$) perpendicular to the bond axis. These are the principal values of the bond polarizability tensor. In our work, we define the polarizability tensor for each bond initially oriented along the z axis.

$$\hat{\alpha}' = \begin{bmatrix} \alpha_{\perp} & 0 & 0 \\ 0 & \alpha_{\perp} & 0 \\ 0 & 0 & \alpha_{\parallel} \end{bmatrix} \tag{4.6}$$

To construct the unit cell polarizability, each bond polarizability needs to be oriented in the direction of the respective bond using a rotation matrix. We can easily compute the rotation matrix if we have two given unit vectors **A** and **B**. When **A** rotates towards **B,** the rotation would be a 2D rotation on a plane with the normal **A**×**B**. We need to first define a unit vector **A** in the positive z-axis corresponding to the initial polarizability tensor

$$\mathbf{A} = \begin{bmatrix} 0 \\ 0 \\ 1 \end{bmatrix} \tag{4.7}$$

Then rotate $\hat{\alpha}$ to align with **B** which would be the direction of each bond in our case. The bond vectors for each bond in the molecule are determined from experiment (or simulation). To determine the required rotation matrix, we need to apply a 2D rotation on **A**, then change the basis of the matrix and shift it to the new orthogonal basis. Hence, the rotation from **A** to **B** in the original base can be expressed as

$$R = F^{-1}GF\ . \tag{4.8}$$

The matrix which represents the rotation is expressed is

$$G = \begin{pmatrix} A.B & -\|A \times B\| & 0 \\ \|A \times B\| & A.B & 0 \\ 0 & 0 & 1 \end{pmatrix} \tag{4.9}$$

and the basis change matrix is represented by **F**

$$F = \left(A \quad \frac{B - (A.B)A}{\left\| B - (A.B)A \right\|} \quad B \times A \right)^{-1}. \tag{4.10}$$

We employ this rotation matrix R onto each bond polarizability and compute the orientation within the unit cell.

$$\hat{\alpha} = R\hat{\alpha}'R^{-1} \tag{4.11}$$

These rotated tensors are summed to yield the unit cell polarizability in eq. (4.5). The sum must also be symmetric because it is the sum of symmetric tensors. Note that the principal axes of the unit cell polarizability are not in general aligned with the unit cell axes. Further, polarizability is an extensive quantity, thus depends on the definition of the unit cell (or molecule).[2-5]

4.3 Construction of the Refractive Index Tensor

The macroscopic intensive property, refractive index n, is related to the microscopic extensive property, molecular polarizability α, by the Lorentz-Lorenz equation.[1, 6-8]

$$\frac{n^2 - 1}{n^2 + 2} = \frac{4}{3}\pi N\alpha, \tag{4.12}$$

where N is the number of molecules per unit volume. The quantity $N\alpha$ can be understood as a polarizability density. For example, the unit cell polarizability divided by the unit cell volume, as we will apply it. Vuks[9] has shown how this relationship can be extended to anisotropic materials with the proper understanding of how the quantities map from the isotropic to the anisotropic case. First the n in the denominator becomes the average refractive index, $\bar{n}$. Second the relationship applies to the principal values of $\hat{\alpha}$ and $\hat{n}$.

In the first step we relate $\bar{\alpha}$ to $\bar{n}$, the arithmetic averages of the principal values of the respective tensors. This is a straightforward application of eq. (4.12) because the average values are scalars.

$$\frac{\bar{n}^2 - 1}{\bar{n}^2 + 2} = \frac{4}{3}\pi N\bar{\alpha} \quad \Rightarrow \quad \bar{n} = \sqrt{\frac{8\pi N\bar{\alpha} + 3}{3 - 4\pi N\bar{\alpha}}} \tag{4.13}$$

The second step relates the principal values, α_i and n_i, using a slightly modified form of Lorentz-Lorenz expression.

$$\frac{n_i^2-1}{\bar{n}^2+2}=\frac{4}{3}\pi N\alpha_i \quad \Rightarrow \quad n_i=\sqrt{\frac{4}{3}\pi N\alpha_i(\bar{n}^2+2)+1} \tag{4.14}$$

In summary, to relate the polarizability and refractive index tensors. The polarizability tensor is first rotated into the coordinate frame that diagonalizes it. The refractive index tensor is calculated. The refractive index tensor is then rotated back into the unit cell coordinate frame. These rotations are the inverse of each other, that is, we rotate the tensor, perform the calculation, then rotate the tensor back.

$$\hat{\alpha} \xleftarrow{R\hat{\alpha}R^{-1}=\hat{\alpha}'} \hat{\alpha}' \Leftrightarrow \hat{n}' \xleftarrow{R^{-1}\hat{n}'R=\hat{n}} \hat{n} \tag{4.15}$$

4.4 Refractive Index Tensor for a *n*-Hexatriacontane Crystal

In this section we test the validity of our method for calculating the refractive index tensor of an anisotropic material, the orthorhombic crystalline phase of *n*-hexatriacontane ($C_{36}H_{74}$). First, we calculate the polarizability tensor for each bond in the unit-cell reference frame and sum them to construct the unit-cell polarizability tensor, $\hat{\alpha}$. After transforming into the principal coordinate frame, $\hat{n}'$ is calculated from $\hat{\alpha}'$. Reversing the rotation returns the refractive index tensor to the unit-cell coordinate frame of the unit cell to obtain $\hat{n}$. Finally, $\hat{n}$ is compared with the experimental values in the literature.

Table 4.1: The unit cell dimension of $C_{36}H_{74}$

a	*b*	*c*
7.42 Å	4.96 Å	95.14 Å

The crystal structure of *n*-hexatriacontane is orthorhombic with unit-cell dimensions is listed in Table 4.1.[10] The alkyl chains are in the all-trans conformation, with the molecular chain axes parallel to the *c* axis. The plane of the molecular chain makes an angle of 43˚ with the *b* axis. For convenience, crystal *c* axis is chosen to be along the *z* axis and the *a*-*b* plane is assumed to be oriented with respect to the *x*-*y* plane in the Cartesian coordinate system. The molecules are arranged in two layers so that the *c* axis is the length of two molecules. Within each layer the C–C–C planes of the two molecules are nearly orthogonal (82°). The atomic coordinates of the carbon atom along with its attached hydrogen atoms of the methylene according to the fractional

coordinate system, except for the coordinates of the third hydrogen atoms of the terminal methyl which are at $n = 0$ and $n = 18$ are listed in Table 4.2(a) and 4.2(b) and similarly the coordinates for the 2nd molecular chain is listed in Table 4.2(c) and 4.2(d). The geometry of the C–H bonds in the methyl group are estimated as follows. First, we take the existing first and last C–C bonds of the molecular chain. For the coordinates of methyl attached to 1st carbon atom, C_1, we extend the C_2–C_1 bond vector in the opposite direction of the bond till the bond length of C–H bond is achieved. Since we already have the coordinates for the other two C–H bonds of the methyl from the literature[10], to obtain the final coordinates of methyl, each of these two C–H bonds were then twisted 120˚with respect to the plane consisting the alkyl chain and similarly the coordinates of the methyl attached to 36th carbon atom is also calculated (see Table 4.2(i)). The coordinates of the carbon atoms associated with the attached hydrogen atoms in the terminal methyl are listed in Table 4.2(e-h). We then construct the unit cell polarizability tensor. De Jong[11] gives the transverse and longitudinal polarizabilities of the C–C and C-H bonds. The polarizability tensor for each C–C and C–H bonds are constructed from these bond polarizabilities using eq. (4.6).[11, 12] The unit cell polarizability tensor is built up by summing the polarizability tensors for each C–C and C–H bond after rotated the initial tensor, eq. (4.12) to orient in the direction for the respective bonds. To demonstrate how the polarizability tensors are rotated along the bond directions, examples of sample C–C and C–H bond directions are shown in Figure 4.1.

Table 4.2: The fractional atomic coordinates of $C_{36}H_{74}$.[10]

(a) For the (2*n*+1)th carbon atoms and its associated hydrogen atoms

Atoms	*x* (Å)	*y* (Å)	*z* (Å)
C	0.014*a*	0.186*b*	(0.01638 + 0.02672*n*)*c*
H_1	0.872*a*	0.206*b*	(0.01638 + 0.02672*n*)*c*
H_2	0.045*a*	0.976*b*	(0.01638 + 0.02672*n*)*c*

(b) For the 2*n*th carbon atoms and its associated hydrogen atoms

Atoms	*x* (Å)	*y* (Å)	*z* (Å)
C	0.092*a*	0.314*b*	{0.02973 + 0.02672(*n*-1)}*c*
H_1	0.061*a*	0.524*b*	{0.02973 + 0.02672(*n*-1)}*c*
H_2	0.234*a*	0.294*b*	{0.02973 + 0.02672(*n*-1)}*c*

(c) For the (2*n*+1)th carbon atoms and its associated hydrogen atoms for the 2nd molecular chain

Atoms	*x* (Å)	*y* (Å)	*z* (Å)
C	0.986*a*	0.186*b*	(0.01638 + 0.02672*n*)*c*
H1	1.128*a*	0.206*b*	(0.01638 + 0.02672*n*)*c*
H2	0.955*a*	0.024*b*	(0.01638 + 0.02672*n*)*c*

(d) For the 2*n*th carbon atoms and its associated hydrogen atoms for the 2nd molecular chain

Atoms	*x* (Å)	*y* (Å)	*z* (Å)
C	0.0908*a*	0.314*b*	{0.02973 + 0.02672(*n*-1)}*c*
H1	0.939*a*	0.524*b*	{0.02973 + 0.02672(*n*-1)}*c*
H2	0.766*a*	0.294*b*	{0.02973 + 0.02672(*n*-1)}*c*

(e) For the methyl attached to 1st carbon atom where $n = 0$, the coordinates of its associated hydrogen atoms

Atoms	*x* (Å)	*y* (Å)	*z* (Å)
H_1	0.28370	1.11980	-0.5908
H_2	1.7340	1.44890	0.23330
H_3	0.47750	2.59430	0.23330

(f) For the methyl attached to 36th carbon atom where n = 18, the coordinates of its associated hydrogen atoms

Atoms	*x* (Å)	*y* (Å)	*z* (Å)
H_1	-0.9476	1.02630	44.83570
H_2	0.3048	-0.11470	44.8360
H_3	0.4974	1.3547	45.6571

(g) For the methyl attached to 1st carbon atom where n = 0, the coordinates of its associated hydrogen atoms for the 2nd molecular chain

Atoms	*x* (Å)	*y* (Å)	*z* (Å)
H_1	-0.2830 + *a*	1.11980	-0.5908
H_2	-1.7340 + *a*	1.44890	0.23330
H_3	-0.47750 + *a*	2.59430	0.23330

(h) For the methyl attached to 36th carbon atom where n = 18, the coordinates of its associated hydrogen atoms for the 2nd molecular chain

Atoms	*x* (Å)	*y* (Å)	*z* (Å)
H_1	0.9476 + *a*	1.02630	44.83570
H_2	0.3048 + *a*	-0.11470	44.8360
H_3	-0.4974 + *a*	1.3547	45.6571

(i) Bond lengths (Å) and bond angles.[10]

Bond lengths (Å)		*Bond angles*	
C–C	1.533	C–C–C	119˚
C–H	1.07	H–C–H	107˚

Table 4.3: Bond polarizabilities (Å^3).[11, 12]

Bond	$\alpha_{\parallel}$	$\alpha_{\perp}$	$\bar{\alpha}$
C–C	0.97	0.25	0.497
C–H	0.78	0.60	0.673

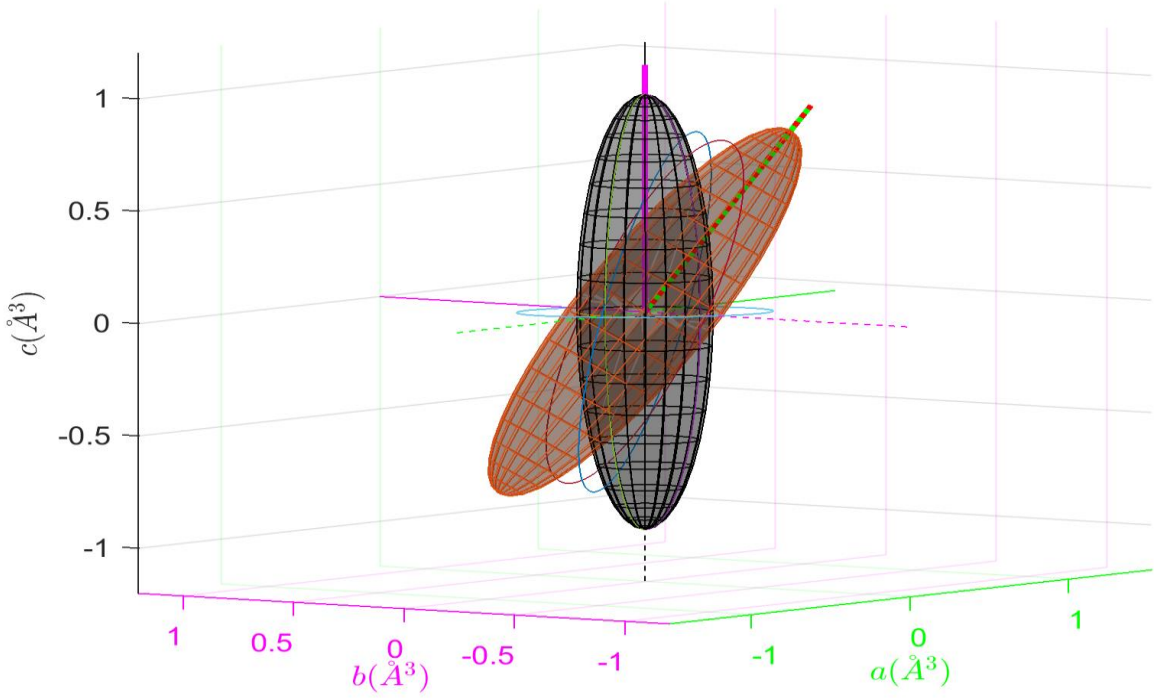

Figure 4.1. Comparison between the initial (black ellipse) and the rotated (orange ellipse) C-C bond polarizability tensor.

In Figure. 4.1, initially at first the C–C bond (magenta line) is oriented along *z*-axis and bond orientation of C–C bond with respect to the unit cell frame is in the *z*-plane (green line). The bond along *z* -axis is rotated towards the oriented bond direction with respect to the laboratory coordinate system. Through this process, we obtain the rotation matrix which we apply on the polarizability tensor along the *z* axis which is the black ellipse. Then rotate it towards the oriented C–C bond and obtain the rotated polarizability tensor. The orange ellipse represents the tensor after it is rotated to align with the C–C bond axis (red/green line). The rotation axis is perpendicular to the plane containing the *z* axis and the C–C bond (green line). Similarly, in this way the rotated polarizability tensors for each C–H bonds can be achieved (Figure 4.2). The polarizability of the unit cell is the sum of these two component

polarizabilities. After obtaining the sum of rotated polarizability tensors for each bond, the unit cell polarizability tensor, $\hat{\alpha}$ for *n*-hexatriacontane is determined (Figure 4.4). Afterwards, the principal values of the diagonalized unit cell polarizability tensor is obtained (Table 4.4).

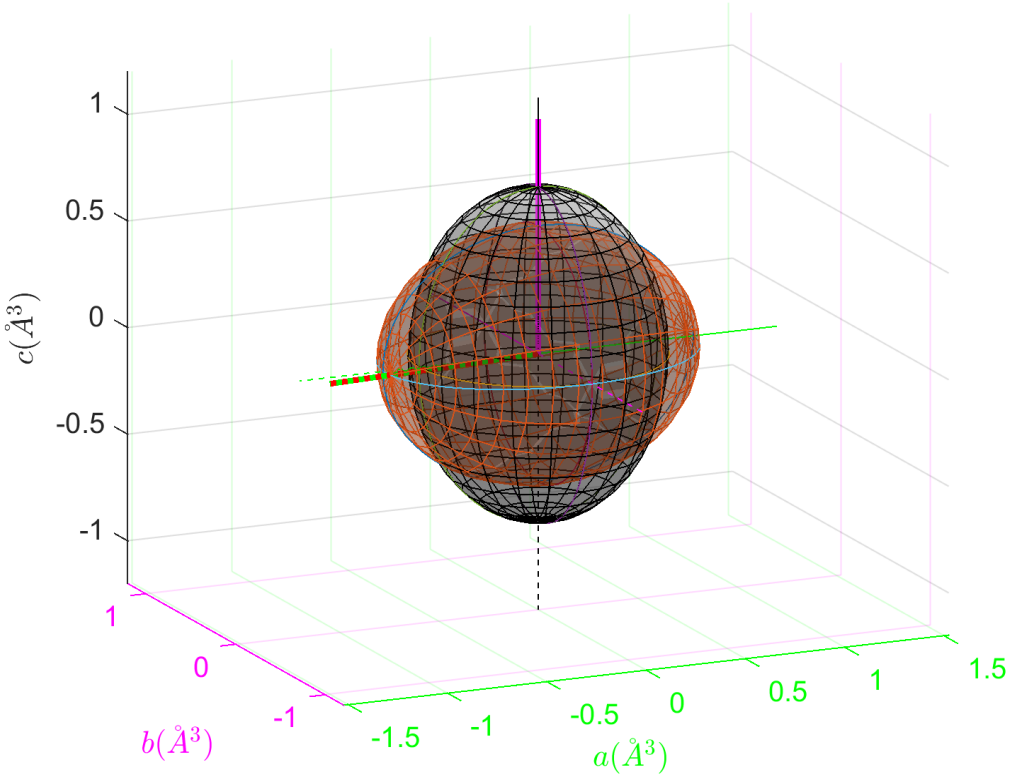

Figure 4.2. Comparison between the initial (black ellipse) and the rotated (orange ellipse) C-C bond polarizability tensor.

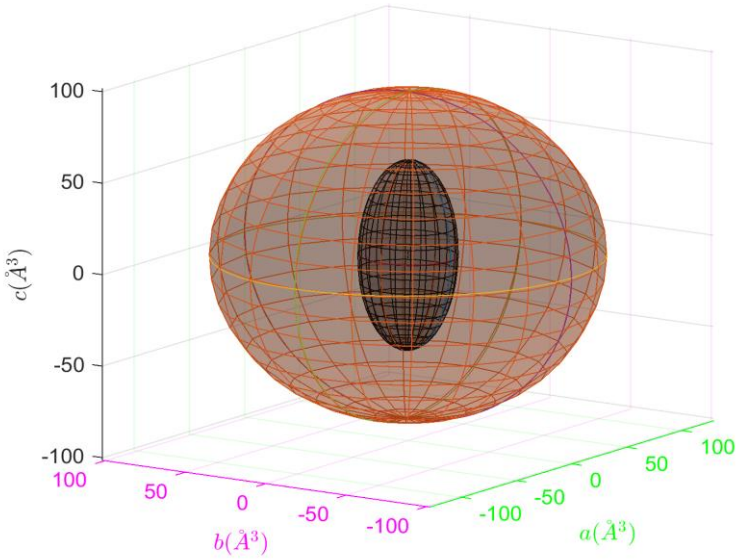

Figure 4.3. The polarizability tensor contributions for the C–C bonds (black ellipse) and C–H bonds (orange ellipse) for orthorhombic *n*-hexatriacontane in the unit-cell reference frame.

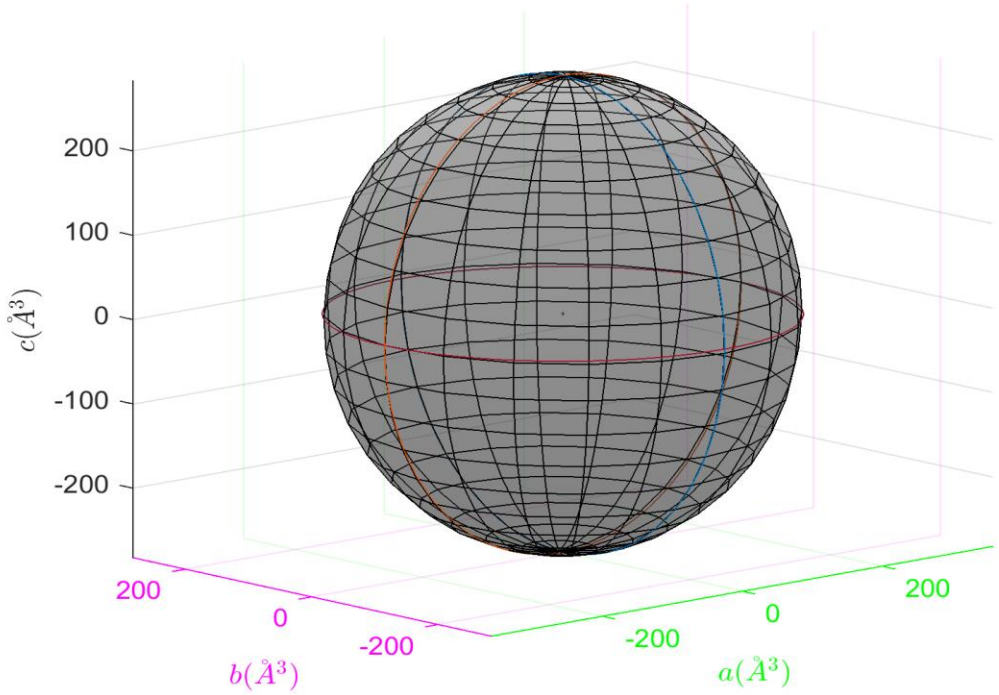

Figure 4.4. The unit cell polarizability tensor, $\hat{\alpha}$ for orthorhombic *n*-hexatriacontane in the unit-cell reference frame.

Table 4.4: The principal values of unit cell polarizability tensor (Å^3)

α_x	α_y	α_z	$\bar{\alpha}$
254	255	282	264

According to eq. (4.13), to calculate the arithmetic average of the principal values, $\bar{n}$ of the refractive index tensor, we need to take the average of the principal values, $\bar{\alpha}$ of the respective polarizability tensor which is,

$$\bar{\alpha} = \frac{\alpha_x + \alpha_y + \alpha_z}{3} \tag{4.16}$$

Applying the calculated $\bar{\alpha}$ in eq. (4.13), we find $\bar{n}$ and the principal values of refractive index tensor. Table 4.5 compares the results to the experimental values.[4]

Table 4.5: The principal values of refractive index tensor for *n*-Hexatriacontane ($C_{36}H_{74}$).

Principal value	*Calculated*	*Experimental.*[4]
n_α	1.5279	1.514
n_β	1.5296	1.519
n_γ	1.5758	1.575

Here, n_α, n_β and n_γ are the principal indices of the crystal. By convention, these are assigned in ascending order of refractive index. Next, the modeled refractive index tensor, $\hat{n}$ is rotated back to the unit cell frame. The shape of the *n*-hexatriacontane crystal studied in the literature is a rhomboidal plate.[10] The longer diagonal of the rhombus shaped crystal plate is along unit cell *a* axis, the shorter diagonal of the plate is along unit cell *b* axis, and the normal to the plate is the unit cell *c* axis. The principal indices of the crystalline refractive index are oriented along the crystal axis. The direction of n_α is along the unit cell *a* axis, n_β is parallel to the *b* axis and n_γ is normal to the plate, *c* axis.

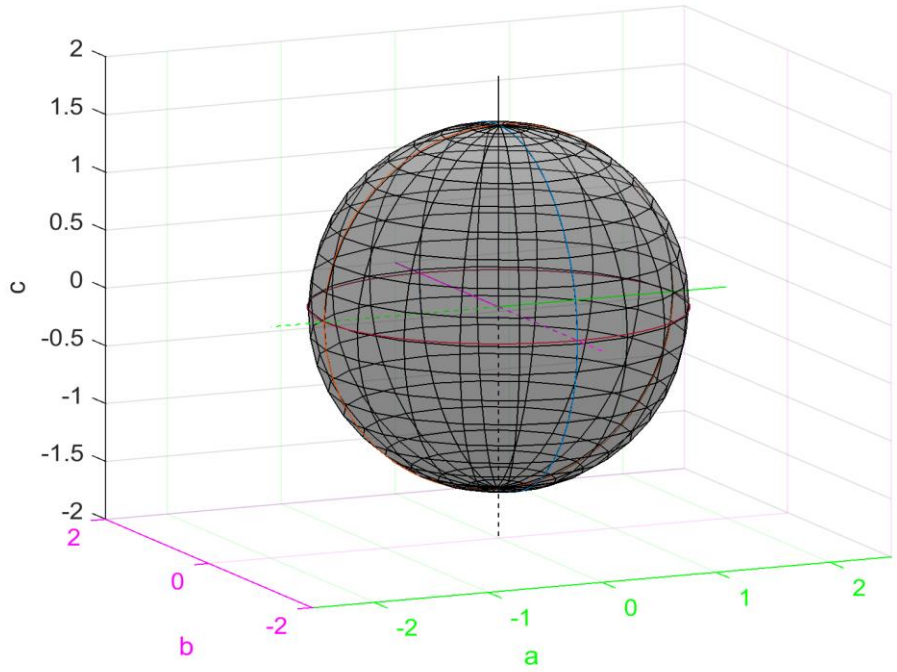

Figure 4.5: The refractive index tensor, $\hat{n}$, for the *n*-hexatriacontane crystal.

Table 4.5 shows that the values that we obtained for n_α, n_β, and n_γ are reasonably in good agreement with the experimental values observed from the literature.[4] The error is within 0.9% for n_α, 0.7% for n_β, and 0.05% for n_γ. In the study by Bunn *et. al*, the bond polarizabilities were obtained from fitting the data to a large number of systems. Hence, they approximated the values of n_α, n_β, and n_γ.[4, 11-13] Since there is always scope for improvement in these kind of approximations and our method approximates the value whose error is within less than 1%, hence, our method to calculate the high frequency refractive index tensor, $\hat{n}_\infty$ is in reasonably good agreement with the experiment.

4.5 Reference

1. Böttcher, C. J. F., *Theory of electric polarisation*. Elsevier Pub. Co.: Amsterdam; Houston, 1952.
2. Denbigh, K. G., The polarisabilities of bonds—I. *Trans. Faraday Soc.* **1940,** *36*, 936-948.
3. Wang, S. N., On the Ellipsoids of Polarization of Bonds and Octets. *J. Chem. Phys.* **1939,** *7* (11), 1012-1015.

4. Bunn, C. W.; Daubeny, R. d. P., The polarizabilities of carbon—carbon bonds. *Trans. Faraday Soc.* **1954,** *50*, 1173-1177.
5. Le Fèvre, R. J. W., Molecular Refractivity and Polarizability. In *Adv. Phys. Org. Chem.*, Gold, V., Ed. Academic Press: 1965; Vol. 3, pp 1-90.
6. Lorentz, H. A., *The theory of electrons and its applications to the phenomena of light and radiant heat*. Germany: B.G. Teubner G.E. Stechert: Germany, 1916.
7. Nussbaum, A.; Phillips, R. A.; Frahm, C. P., Contemporary Optics for Scientists and Engineers. *Phys. Today* **1977,** *30* (5), 74-76.
8. Sylvester-Hvid, K. O.; Åstrand, P.-O.; Ratner, M. A.; Mikkelsen, K. V., Frequency-Dependent Molecular Polarizability and Refractive Index: Are Substituent Contributions Additive? *J. Phys. Chem. A* **1999,** *103* (12), 1818-1821.
9. Vuks, M. F., Determination of the Optical Anisotropy of Aromatic Molecules from the Double Refraction of Crystals. *Opt. Spectrosc.* **1966,** *20*, 361.
10. Teare, P., The crystal structure of orthorhombic hexatriacontane, $C_{36}H_{74}$. *Acta Cryst.* **1959,** *12* (4), 294-300.
11. De Jong, S., Groeneweg, F.; Van Voorst Vader, F., Calculation of the refractive indices of molecular crystals. *J. Appl. Crystallogr.* **1991,** *24* (2), 171-174.
12. In ref.[11], the bond polarizabilities listed in table (1) are reported in wrong order. The average polarizability should be listed in the longitudinal column and vice versa. Also, the units of bond polarizabilities should be in Å3. .
13. Winchell, A. N., *The optical properties of organic compounds*. Madison, The University of Wisconsin Press: Madison, 1943.

Chapter 5
4×4 Transfer Matrix Method

In order to study the optical properties of the anisotropic medium, the 4×4 matrix formalism is a powerful tool to describe light wave propagation through stratified anisotropic media. In this chapter, a general description of the 4×4 transfer matrix is presented. This 4×4 matrix formalism is particularly well-suited for calculating the reflectance of anisotropic films on gold needed for our project. The algorithm of this matrix formulation has been implemented directly in a computer program. It starts with a 6×6 matrix representation of Maxwell's equations which includes optical rotations (Faraday rotation, circular birefringence, and more) and later reduces to a 4×4 representation. A description of the relevant electromagnetic theory (EM) and formulation of the 4×4 transfer matrix technique is first summarized. We then vet the published 4×4 code published by Passler and Paarmann by comparing it to Fresnel's equations for a three-layer isotropic system.

5.1 Background of 4×4 Transfer Matrix Method

Treatment of the electromagnetic wave propagation through a layered stack (stratified media) depends on the symmetry. Transfer matrix methods are used to model the propagation of EM waves in stratified media. In these methods, the properties of each layer are described by an interfacial matrix and a propagation matrix. The transmission and reflection of the stack are found by multiplying the matrices for all the layers in the stack. In this way the transfer matrix method can be easily extended to any number of layers. The most general methods formulated the problem in terms of 4×4 matrices. Two modes propagating into the stack (the transmitted waves) and two modes propagating out of the stack (the reflected waves).

We can divide optical materials broadly into isotropic and anisotropic, and the latter into sub-types of uniaxial and biaxial. In isotropic materials the three principal components of the refractive index are equal, thus can be treated as a scalar. For anisotropic materials, the refractive index is a tensor. If two of the principal components are equal, the material is termed uniaxial. If all three are unique, the material is termed biaxial. The optics of anisotropic materials are more

complex because for any given direction of propagation direction in the crystal there exist two orthogonal polarizations each with its own phase velocity. The orientation of these planes of polarization is determined by the symmetry and orientation of the crystal. In uniaxial crystals these two modes are termed the ordinary ray (o-ray), with its electric field perpendicular to the optic axis, and the extraordinary ray (e-ray), with its plane of polarization containing the direction of propagation and the optic axis. The o-ray obeys Snell's law, with its wave vector and ray vector in parallel. The e-ray does not obey Snell's law, thus the wave vector and the ray vectors are not parallel. The odd behavior of the e-ray is a manifestation of the fact that **E** and **D** are not in general parallel in anisotropic materials. In biaxial crystals both rays are in general e-rays.

When only isotropic media are involved, the plane of reflection provides a reference frame that divides the problem into two orthogonal linearly polarized modes, viz. transverse electric (TE) and transverse magnetic (TM). The phase velocity of the TE and TM modes are the same in isotropic media, as determined by the refractive index. This problem contains TE and TM waves propagating into the stack (the transmitted waves) and TE and TM waves propagating out of the stack (reflected waves). For ideal materials and interfaces, there is no mode mixing between the TE and TM modes. Therefore, the problem can be separated into two independent problems, one for the TE transmitted and reflected waves and another for TM. This simplifies the 4×4 transfer matrix problem into two uncoupled 2×2 transfer matrix problems.

If one or more of the media in the stack are anisotropic, the problem can no longer be separated and the handy distinction of TE and TM polarization is no longer valid. The anisotropic media now impose their own additional symmetry to the problem. This is because for any given direction of propagation direction in the crystal there exist two orthogonal polarizations each with the own phase velocity. The orientation of these planes of polarization is determined by the symmetry and orientation of the crystal. The boundary conditions at the interfaces retain the basic TE and TM symmetry. The result is that the mode mixing can be significant and the full 4×4 transfer matrix is required.

Jones[1] and Abelès[2, 3] developed 2×2 matrix methods for stratified isotropic material. Extension to stratified anisotropic media, where the symmetry of the medium is low, requires a 4×4 matrix technique was first introduced by Teitler and Henvis[4] where all the field variables, (e.g., two electric and two magnetic fields) throughout the computation were employed to solve

the problem. In recent years, the phenomena of the generalized theory of propagated electromagnetic wave for stratified anisotropic media has been studied by several workers.[5-8] The 4×4 transfer matrix formalism developed by Berreman[9] and Yeh[6-8] have been founded to be the most complete among all these studies. Yeh's formalism was adopted by Parikh and Allara[10] so it was the approach we first tried to employ. Unfortunately it suffers from singularities due to optical degeneracies.[11] Berreman's method has been found to be more tractable.[11] Mathematically, solving for the modes in each layer is a separate quartic eigenvalue problem. The challenge is to consistently assign the eigen modes of each layer to its 4×4 matrix. (The failure to do this properly, is termed "discontinuities" in the literature.[12]) Since we began this work, Passler and Paarmann published a 4×4 matrix formalism and its Matlab implementation using Berreman's method.[9, 12] Their algorithm eliminates any numerical instabilities and discontinuities and can accommodate any number of arbitrarily isotropic or anisotropic layers. In the following section, we summarize the method.

5.2 Implementation of 4×4 Transfer Matrix Method

A multilayered thin film structure consisting of *N* semi-infinite planar slabs where each layer has a definite thickness, d_i, is modelled here. The light propagating through the stratified layered media is an infinite homogeneous, monochromatic plane wave with a frequency, ω. The magnetic permeability, μ is considered as a scalar. The coordinate system is oriented with the *z*-axis perpendicular to the slab. The incident beam, originating in layer 0, propagates toward the slab and the multilayer surface is parallel to the *xy*-plane. The angle of incidence on the sample is θ. The plane of incidence is the azimuthal angle, ϕ, from the coordinate system. The thickness of each layer is d_i. Each layer of medium has an individual dielectric tensor, $\hat{\varepsilon}$. In this treatment, the initial medium is isotropic. The incident wave is propagating in the *xz*-plane with a wave vector $\vec{k}$,

$$\vec{k} = \frac{\omega}{c}(\xi, 0, q) \tag{5.1}$$

where, the x-component of $\vec{k}$ is $\xi = \sqrt{\varepsilon}\sin\theta$ and the *z*-component of the wave vector scaled by ω/c is *q*, thus dimensionless. The transverse wavevector ξ, also scaled by ω/c, is conserved throughout the multilayer medium (momentum conservation).

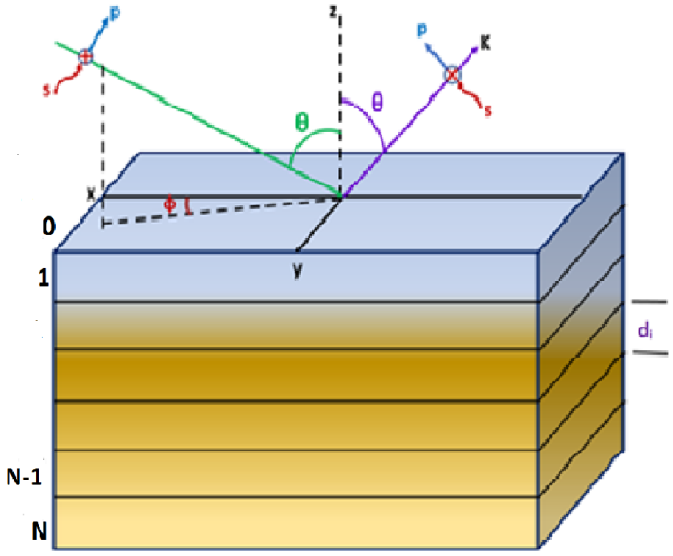

Figure 5.1: N semi-infinite parallel-layer sample of definite thickness, d_i. The light beam enters the surface of phase 1 at an incidence angle, θ and with an azimuthal angle, φ in the *xz* plane. The direction of the electric field for s and p polarization for the incident and reflected beam are shown. The propagation vector, *k* for the reflected beam is also shown.

If the system is described with a diagonal dielectric tensor that is symmetric with principal dielectric constants ε_x, ε_y and ε_z, then the crystal orientation can be rotated along the lab frame

$$\hat{\varepsilon} = R\hat{\varepsilon}'R^{-1} = R\begin{pmatrix} \varepsilon_x & 0 & 0 \\ 0 & \varepsilon_x & 0 \\ 0 & 0 & \varepsilon_x \end{pmatrix}R^{-1} \quad , \tag{5.2}$$

where *R* is the rotation matrix defined in eqs. (4.8).

We will briefly summarize the problem presented by Berreman[9] and by Passler and Paarmann.[12] Generally, there is are four eigenmodes which are the four possible solutions for the propagating electromagnetic wave for each layer. Maxwell's equations are written in Gaussian units in the 6x6 matrix form,

$$\vec{R}\vec{G} \equiv \begin{pmatrix} 0 & 0 & 0 & 0 & -\frac{\partial}{\partial z} & \frac{\partial}{\partial y} \\ 0 & 0 & 0 & \frac{\partial}{\partial z} & 0 & -\frac{\partial}{\partial x} \\ 0 & 0 & 0 & -\frac{\partial}{\partial y} & -\frac{\partial}{\partial x} & 0 \\ 0 & \frac{\partial}{\partial z} & -\frac{\partial}{\partial y} & 0 & 0 & 0 \\ -\frac{\partial}{\partial z} & 0 & -\frac{\partial}{\partial z} & 0 & 0 & 0 \\ \frac{\partial}{\partial y} & -\frac{\partial}{\partial x} & 0 & 0 & 0 & 0 \end{pmatrix} \begin{pmatrix} E_x \\ E_y \\ E_z \\ H_x \\ H_y \\ H_z \end{pmatrix} = \frac{1}{c}\frac{\partial}{\partial t} \begin{pmatrix} D_x \\ D_y \\ D_z \\ B_x \\ B_y \\ B_z \end{pmatrix} \equiv \frac{1}{c}\frac{\partial}{\partial t}\vec{C} \quad . \tag{5.3}$$

where the electromagnetic field vectors are denoted by **E**, **H**, **D** and **B** and the velocity of light in vacuum is *c*. **R** is a symmetric matrix with four quadrants. The first quadrant is the **curl** operator on **H**. The third quadrant is the negative **curl** operator on **E**. After performing the time derivative, Maxwell's equation in the abbreviated form becomes

$$\vec{R}\vec{G} = -\frac{i\omega}{c}\vec{C} \quad . \tag{5.4}$$

A linear relation between **G** and **C** can be written as follows:

$$\vec{C} = \vec{M}\vec{G} \equiv \begin{pmatrix} \hat{\varepsilon} & \hat{\rho}_1 \\ \hat{\rho}_2 & \hat{\mu} \end{pmatrix} \vec{G} \quad . \tag{5.5}$$

Here, $\hat{\rho}_1$ and $\hat{\rho}_2$ of **M** are optical rotation tensors in the first and third quadrants

$$\rho_{1ij} = M_{i,j+3} \tag{5.6}$$

and $$\rho_{2ij} = M_{i+3,j}\,,\ i, j = 1, 2, 3 \tag{5.7}$$

The dielectric tensor, $\hat{\varepsilon}$ is in the second

$$\varepsilon_{ij} = M_{ij}\,,\ i, j = 1, 2, 3 \tag{5.8}$$

Lastly, the permeability tensor, $\hat{\mu}$ is in the fourth quadrant

$$\mu_{ij} = M_{i+3,j+3}\,,\ i, j = 1, 2, 3 \tag{5.9}$$

By combining eq. (5.4) and (5.5),

$$\vec{R}\vec{g} = -\frac{i\omega}{c}\vec{M}\vec{g} \tag{5.10}$$

where **g** is the spatial part of **G** such as, $\vec{G} = \vec{g}\exp(-i\omega t)$.

A classical treatment of wave propagation in optically active isotropic media was described by Drude[13]:

$$\nabla \times \vec{E} = -\frac{1}{c}\frac{\partial \vec{H}}{\partial t} \tag{5.11}$$

and
$$-\left(\nabla \times \vec{H}\right) = -\frac{\varepsilon}{c}\frac{\partial \vec{E}}{\partial t} + \frac{\gamma}{c}\frac{\partial}{\partial t}\left(\nabla \times \vec{E}\right), \tag{5.12}$$

where both ε and γ in general dependent on frequency. We eliminate **curl E** from eq. (5.12) and incorporate the time dependence. Hence the equations become,

$$\nabla \times \vec{E} = \frac{i\omega \vec{H}}{c} \tag{5.13}$$

and
$$-\left(\nabla \times \vec{H}\right) = i\omega\varepsilon\vec{E}/c - \left(i\omega\gamma/c\right)\left(i\omega\vec{H}/c\right) \tag{5.14}$$

Comparing equations (5.13) and (5.14) to equations from (5.6) to (5.10) it can be shown that, the four quadrants of **M** are

$$\begin{aligned} \hat{\rho}_1 &= \left(i\omega\gamma/c\right)\vec{I} \\ \hat{\varepsilon} &= \varepsilon\vec{I} \\ \hat{\rho}_2 &= \vec{\mathrm{O}} \\ \mu &= \vec{I} \end{aligned} \tag{5.15}$$

Here, the identity matrix is denoted as **I** and the null matrix as **O**.

To pursue the solution of eq. (5.4), we need to write up a special form of the first quadrant of **R** which contains the **curl** operator,

$$R_1 = \begin{pmatrix} 0 & -\frac{\partial}{\partial z} & 0 \\ \frac{\partial}{\partial z} & 0 & -i\xi \\ 0 & i\xi & 0 \end{pmatrix} \tag{5.16}$$

and the third quadrant which is $-$**curl** i.e., the transpose of $\mathbf{R}_1$ is denoted by $\mathbf{R}_3$.

After substituting eq. (5.16) into (5.4), it is observed that among the six components of **g**, the normal field projections, $g_3 = E_z$ and $g_6 = H_z$ can be solved in terms of the other four components and hence, can be eliminated. Therefore, the other four first-order linear differential equations from eqs. (5.4) and (5.16) take the forms:

$$-\frac{ic}{\omega}\frac{\partial}{\partial z} g_5 = \sum_{i=1}^{6} M_{1i} g_i \tag{5.17}$$

$$-\frac{ic}{\omega}\frac{\partial}{\partial z} g_4 = \sum_{i=1}^{6} M_{2i} g_i - \frac{c\xi}{\omega} g_6 \tag{5.18}$$

$$-\frac{ic}{\omega}\frac{\partial}{\partial z} g_2 = \sum_{i=1}^{6} M_{4i} g_i \tag{5.19}$$

and

$$-\frac{ic}{\omega}\frac{\partial}{\partial z} g_1 = \sum_{i=1}^{6} M_{5i} g_i + \frac{c\xi}{\omega} g_3 \tag{5.20}$$

The two linear algebraic equations may be written as

$$-\left(c\xi/\omega\right) g_5 = \sum_{i=1}^{6} M_{3i} g_i$$

and (5.21)

$$-\left(c\xi/\omega\right) g_2 = \sum_{i=1}^{6} M_{6i} g_i$$

Solving for g_3 and g_6 in terms of the other parameters give

$$g_3 = a_{31} g_1 + a_{32} g_2 + a_{34} g_4 + a_{35} g_5$$

and (5.22)

$$g_6 = a_{61} g_1 + a_{62} g_2 + a_{64} g_4 + a_{65} g_5$$

where

$$
\begin{aligned}
a_{31} &= \left(M_{61}M_{36} - M_{31}M_{66}\right)/d\,,\\
a_{32} &= \left\{\left(M_{62} - \xi\right)M_{36} - M_{32}M_{66}\right\}/d\,,\\
a_{34} &= \left(M_{64}M_{36} - M_{34}M_{66}\right)/d\,,\\
a_{35} &= \left\{M_{65}M_{36} - \left(M_{35} + \xi\right)M_{66}\right\}/d\,,\\
a_{61} &= \left(M_{63}M_{31} - M_{33}M_{61}\right)/d\,,\\
a_{62} &= \left\{M_{63}M_{32} - M_{33}\left(M_{62} - \xi\right)\right\}/d\,,\\
a_{64} &= \left(M_{63}M_{34} - M_{33}M_{64}\right)/d\,,\\
a_{65} &= \left\{M_{63}\left(M_{35} + \xi\right) - M_{33}M_{65}\right\}/d\\
a_{33} &= a_{36} = a_{63} = a_{66} = 0
\end{aligned}
\tag{5.23}
$$

and

$$d = M_{33}M_{66} - M_{36}M_{63}\,. \tag{5.24}$$

In order to eliminate g_3 and g_6 and to have four first-order differential equations, it is required to substitute both the eqs. (5.22) and (5.23) into eqs. (5.17-20) so that these four linear combinations can be written in 4×4 matrix form as

$$-\frac{ic}{\omega}\frac{\partial}{\partial z}\begin{pmatrix} 0 & 0 & 0 & 1\\ 0 & 0 & -1 & 0\\ 0 & -1 & 0 & 0\\ 1 & 0 & 0 & 0 \end{pmatrix}\begin{pmatrix} E_x\\ E_y\\ H_x\\ H_y \end{pmatrix} = s\begin{pmatrix} E_x\\ E_y\\ H_x\\ H_y \end{pmatrix} \quad . \tag{5.25}$$

To get an equivalent equation like eq. (5.24), it is convenient to change the order of the variables and sign on H_x by multiplying the matrix from the left side of eq. (5.24) by its own inverse matrix which becomes

$$\frac{\partial}{\partial z}\begin{pmatrix} E_x\\ E_y\\ H_x\\ H_y \end{pmatrix} = \frac{i\omega}{c}\begin{pmatrix} S_{41} & S_{44} & S_{42} & -S_{43}\\ S_{11} & S_{14} & S_{12} & -S_{13}\\ -S_{31} & -S_{34} & -S_{32} & S_{33}\\ S_{21} & S_{24} & S_{22} & -S_{13} \end{pmatrix}\begin{pmatrix} E_x\\ H_y\\ E_y\\ -H_x \end{pmatrix} \quad , \tag{5.26}$$

which can be abbreviated as,

$$\frac{\partial}{\partial z}\psi = i\frac{\omega}{c}\Delta\psi \tag{5.27}$$

where the dimensionless field vector is,

$$\psi = \begin{pmatrix} E_x \\ H_y \\ E_y \\ -H_x \end{pmatrix} \tag{5.28}$$

Therefore, the elements of Δ are defined exactly defined in terms of **M** and obtained from eqs. (5.17-20), (5.22) and (5.23),

$$\begin{aligned}
\Delta_{11} &= M_{51} + \left(M_{53} + \xi\right) a_{31} + M_{56} a_{61}, \\
\Delta_{12} &= M_{55} + \left(M_{53} + \xi\right) a_{35} + M_{56} a_{65}, \\
\Delta_{13} &= M_{52} + \left(M_{53} + \xi\right) a_{32} + M_{56} a_{62}, \\
\Delta_{14} &= -M_{54} - \left(M_{53} + \xi\right) a_{34} - M_{56} a_{64}, \\
\Delta_{21} &= M_{11} + M_{13} a_{31} + M_{16} a_{61}, \\
\Delta_{22} &= M_{15} + M_{13} a_{35} + M_{16} a_{65}, \\
\Delta_{23} &= M_{12} + M_{13} a_{32} + M_{16} a_{62}, \\
\Delta_{24} &= -M_{14} - M_{13} a_{34} - M_{16} a_{64}, \\
\Delta_{31} &= -M_{41} - M_{43} a_{31} - M_{46} a_{61}, \\
\Delta_{32} &= -M_{45} - M_{43} a_{35} - M_{46} a_{65}, \\
\Delta_{33} &= -M_{42} - M_{43} a_{32} - M_{46} a_{62}, \\
\Delta_{34} &= M_{44} + M_{43} a_{34} + M_{46} a_{64}, \\
\Delta_{41} &= M_{21} + M_{23} a_{31} + \left(M_{26} - \xi\right) a_{61}, \\
\Delta_{42} &= M_{25} + M_{23} a_{35} + \left(M_{26} - \xi\right) a_{65}, \\
\Delta_{43} &= M_{22} + M_{23} a_{32} + \left(M_{26} - \xi\right) a_{62}, \\
\Delta_{44} &= M_{24} + M_{23} a_{34} + \left(M_{26} - \xi\right) a_{64},
\end{aligned} \tag{5.29}$$

The four eigenvalues of Δ are represented by the *z*-components of the wave vectors of the four eigenmodes in the structure

$$q_{ij} \Delta(i) = \psi_{ij} \Delta(i) \tag{5.30}$$

where, q_{ij} are the eigenvalues indexed *j* for each layer *i*, and the eigenmodes as ψ_{ij} in the medium. To ignore unstable solutions and any discontinuities, the four solutions need to be ordered in an explicit manner. First, the modes are required to be divided into two parts, e.g. transmitted (forward) and reflected (backward) propagating waves. Transmitted wave correspond to the

modes with $q_{ij} \geq 0$ and $\mathrm{Im}\left(q_{ij}\right) \geq 0$ and reflected modes to $q_{ij} < 0$ and $\mathrm{Im}\left(q_{ij}\right) < 0$. The modes are sorted in this way because real wave vectors point in the direction of propagation and exponentially damped waves are defined by complex wave vectors. Moreover, it needs to be determined that the solutions are computed without any discontinuities. q_{i1}, q_{i2} are referred to the transmitted waves, and q_{i3}, q_{i4} are referred to the reflected waves. Hence, the eigenvectors of eq. (5.30) of each layer may be written as follows[14],

$$C(q_{ij}) = \frac{\left|\psi_{ij1}\right|^2}{\left|\psi_{ij1}\right|^2 + \left|\psi_{ij3}\right|^2} \tag{5.31}$$

Finally, the four eigenvalues are sorted in the following way where q_{i1} and q_{i3} are described as the *p*-polarized, and q_{i2} and q_{i4} are the *s*-polarized waves, transmitted and reflected, respectively,

$$C\left(q_{i1}\right) > C\left(q_{i2}\right) \text{ and } C\left(q_{i3}\right) > C\left(q_{i4}\right) \tag{5.32}$$

For birefringent media where there is at least one principal axis which is neither in the *xz*-plane or along the *y*-axis in the anisotropic dielectric tensor, discontinuity can arise. In such cases, instead of analyzing electric fields, Poynting vector needs to be used in eq. (5.31),

$$C(q_{ij}) = \frac{\left|S_{ijx}\right|^2}{\left|S_{ijx}\right|^2 + \left|S_{ijy}\right|^2} \tag{5.33}$$

where,

$$S_{ij} = \begin{pmatrix} S_{ijx} \\ S_{ijy} \\ S_{ijz} \end{pmatrix} = \vec{E}_{ij} \times \vec{H}_{ij} = \begin{pmatrix} E_{ijy}H_{ijz} - E_{ijz}H_{ijy} \\ E_{ijz}H_{ijx} - E_{ijx}H_{ijz} \\ E_{ijx}H_{ijy} - E_{ijy}H_{ijx} \end{pmatrix} \tag{5.34}$$

Comparing with eq. (5.28), $E_{ijx} = \psi_{ij1}, E_{ijy} = \psi_{ij3}, H_{ijx} = -\psi_{ij4}, H_{ijy} = \psi_{ij2}$,

and
$$\begin{aligned} E_{ijz} &= a_{31}(i)E_{ijx} + a_{32}(i)E_{ijy} + a_{34}(i)H_{ijx} + a_{35}(i)H_{ijy}, \\ H_{ijz} &= a_{61}(i)E_{ijx} + a_{62}(i)E_{ijy} + a_{64}(i)H_{ijx} + a_{65}(i)H_{ijy} \end{aligned} \tag{5.35}$$

In order to deal with singularities, the study presented by Xu *et al*. was employed.[11] The method from their study was applied in the case of non-optically active media with isotropic magnetic permeability and to match that approach, the matrix from eq. (5.5) was set up as,

$\hat{\mu} = \mu\vec{I}$ and $\hat{\rho}_1 = \hat{\rho}_2 = \vec{\mathrm{O}}$, with **I** and **O** as the unity and null matrix. Then the electric field vectors $\boldsymbol{\gamma}$ of the four eigenmodes for each layer *i* was set up in order to set up the transfer matrix corresponding to where the q_{ij} are sorted accordingly

$$\vec{\gamma}_{ij} = \begin{pmatrix} \gamma_{ij1} \\ \gamma_{ij2} \\ \gamma_{ij3} \end{pmatrix}. \tag{5.36}$$

Therefore, the values which are free of singularities in γ_{ijk} are written in the following forms

$$\gamma_{i11} = \gamma_{i22} = \gamma_{i42} = -\gamma_{i31} = 1,$$

$$\gamma_{i12} = \begin{cases} 0, q_{i1} = q_{i2} \\ \dfrac{\mu_i\varepsilon_{i23}\left(\mu_i\varepsilon_{i31} + \xi q_{i1}\right) - \mu_i\varepsilon_{i21}\left(\mu_i\varepsilon_{i33} - \xi^2\right)}{\left(\mu_i\varepsilon_{i33} - \xi^2\right)\left(\mu_i\varepsilon_{i22} - q_{i1}^2\right) - \mu_i^2\varepsilon_{i23}\varepsilon_{i32}}, q_{i1} \neq q_{i2} \end{cases}$$

$$\gamma_{i13} = \begin{cases} -\dfrac{\mu_i\varepsilon_{i31} + \xi q_{i1}}{\mu_i\varepsilon_{i33} - \xi^2}, q_{i1} = q_{i2} \\ -\dfrac{\mu_i\varepsilon_{i31} + \xi q_{i1}}{\mu_i\varepsilon_{i33} - \xi^2} - -\dfrac{\mu_i\varepsilon_{i32}}{\mu_i\varepsilon_{i33} - \xi^2}, q_{i1} \neq q_{i2} \end{cases}$$

$$\gamma_{i21} = \begin{cases} 0, q_{i1} = q_{i2} \\ \dfrac{\mu_i\varepsilon_{i32}\left(\mu_i\varepsilon_{i13} + \xi q_{i2}\right) - \mu_i\varepsilon_{i12}\left(\mu_i\varepsilon_{i33} - \xi^2\right)}{\left(\mu_i\varepsilon_{i33} - \xi^2\right)\left(\mu_i\varepsilon_{i11} - q_{i2}^2\right) - \left(\mu_i\varepsilon_{i13} + \xi q_{i2}\right)\left(\mu_i\varepsilon_{i31} + \xi q_{i2}\right)}, q_{i1} \neq q_{i2} \end{cases}$$

$$\gamma_{i23} = \begin{cases} -\dfrac{\mu_i\varepsilon_{i32}}{\mu_i\varepsilon_{i33} - \xi^2}, q_{i1} = q_{i2} \\ -\dfrac{\mu_i\varepsilon_{i31} + \xi q_{i2}}{\mu_i\varepsilon_{i33} - \xi^2}\gamma_{i21} - \dfrac{\mu_i\varepsilon_{i32}}{\mu_i\varepsilon_{i33} - \xi^2}, q_{i1} \neq q_{i2} \end{cases}$$

$$\gamma_{i32} = \begin{cases} 0, q_{i3} = q_{i4} \\ \dfrac{\mu_i\varepsilon_{i21}\left(\mu_i\varepsilon_{i33} + \xi^2\right) - \mu_i\varepsilon_{i23}\left(\mu_i\varepsilon_{i31} - \xi q_{i3}\right)}{\left(\mu_i\varepsilon_{i33} - \xi^2\right)\left(\mu_i\varepsilon_{i22} - -\xi^2 - q_{i3}^2\right) - \mu_i^2\varepsilon_{i23}\varepsilon_{i32}}, q_{i3} \neq q_{i4} \end{cases}$$

$$\gamma_{i33}=\begin{cases}\dfrac{\mu_i\varepsilon_{i31}+\xi q_{i3}}{\mu_i\varepsilon_{i33}-\xi^2}, q_{i3}=q_{i4}\\ \dfrac{\mu_i\varepsilon_{i31}+\xi q_{i2}}{\mu_i\varepsilon_{i33}-\xi^2}+\dfrac{\mu_i\varepsilon_{i32}}{\mu_i\varepsilon_{i33}-\xi^2}, q_{i3}\neq q_{i4}\end{cases}$$

$$\gamma_{i41}=\begin{cases}0, q_{i3}=q_{i4}\\ \dfrac{\mu_i\varepsilon_{i32}\left(\mu_i\varepsilon_{i31}+\xi q_{i4}\right)-\mu_i\varepsilon_{i12}\left(\mu_i\varepsilon_{i33}-\xi^2\right)}{\left(\mu_i\varepsilon_{i33}-\xi^2\right)\left(\mu_i\varepsilon_{i11}-q_{i4}^2\right)-\left(\mu_i\varepsilon_{i13}+\xi q_{i4}\right)\left(\mu_i\varepsilon_{i31}+\xi q_{i4}\right)}, q_{i3}\neq q_{i4}\end{cases}$$

$$\gamma_{i23}=\begin{cases}-\dfrac{\mu_i\varepsilon_{i32}}{\mu_i\varepsilon_{i33}-\xi^2}, q_{i3}=q_{i4}\\ -\dfrac{\mu_i\varepsilon_{i31}+\xi q_{i4}}{\mu_i\varepsilon_{i33}-\xi^2}\gamma_{i41}-\dfrac{\mu_i\varepsilon_{i32}}{\mu_i\varepsilon_{i33}-\xi^2}, q_{i3}\neq q_{i4}\end{cases} \tag{5.37}$$

All these solutions are continuous and finite for both anisotropic and isotropic media. Hence, they formulated a generalized and stable transfer matrix using these solutions. To achieve that, boundary conditions between two adjacent layers *i* and *i*-1 are applied for electric and magnetic fields for all four modes simultaneously,

$$A_{i-1}\vec{E}_{i-1}=A_i\vec{E}_i \tag{5.38}$$

where A_i is computed using γ_{ijk} by ref. [11],

$$A_i=\begin{pmatrix}\gamma_{i11} & \gamma_{i21} & \gamma_{i31} & \gamma_{i41}\\ \gamma_{i12} & \gamma_{i22} & \gamma_{i32} & \gamma_{i42}\\ \dfrac{q_{i1}\gamma_{i11}-\xi\gamma_{i13}}{\mu_i} & \dfrac{q_{i2}\gamma_{i21}-\xi\gamma_{i23}}{\mu_i} & \dfrac{q_{i3}\gamma_{i31}-\xi\gamma_{i33}}{\mu_i} & \dfrac{q_{i4}\gamma_{i41}-\xi\gamma_{i43}}{\mu_i}\\ \dfrac{1}{\mu}q_{i1}\gamma_{i12} & \dfrac{1}{\mu}q_{i2}\gamma_{i22} & \dfrac{1}{\mu}q_{i3}\gamma_{i32} & \dfrac{1}{\mu}q_{i4}\gamma_{i42}\end{pmatrix} \tag{5.39}$$

Furthermore, the electric field for the whole multilayered structure, the dimensionless four-component electric field vector of the solution is

$$\vec{E}\equiv\begin{pmatrix}E_t^p\\ E_t^s\\ E_r^p\\ E_r^s\end{pmatrix}, \tag{5.40}$$

where, the in-plane field amplitudes of the *s* and *p*-polarized, transmitted and reflected fields, are represented by, $E_t^{s(p)}$ and $E_r^{s(p)}$. From both sides of eq. (5.38), $\boldsymbol{A}_i^{-1}$ is multiplied to obtain the following relation where the interface matrix $\mathbf{L}_i$ is described explicitly

$$\vec{E}_{i-1} = A_{i-1}^{-1} A_i \vec{E}_i \equiv L_i \vec{E}_i \tag{5.41}$$

It becomes clear after analyzing eq. (5.39) that the columns from matrix A_i resemble with four eigenmodes ψ_{ij} of each respective layer, although the elements now have the order of E_x, E_y, H_x and H_y. Hence, the solution of the electric field vector which is projected onto the eigenmodes of the layer is represented by the matrix operation of $A_i\vec{E}_i$, while the projection of the eigenmodes in layer *i* onto those of layer *i*-1 is being depicted by $\mathbf{L}_i$. The different order of the elements from the column vector must be taken into account after comparing with eq. (5.36). This can be achieved after the transfer matrix is formulated for the full multilayer structure.

The propagation matrix, P_i from Yeh [6] contains the phase factor due to propagation through each layer.

$$P_i = \begin{pmatrix} \exp\left(-i\frac{\omega}{c} q_{i1} d_i\right) & 0 & 0 & 0 \\ 0 & \exp\left(-i\frac{\omega}{c} q_{i2} d_i\right) & 0 & 0 \\ 0 & 0 & \exp\left(-i\frac{\omega}{c} q_{i3} d_i\right) & 0 \\ 0 & 0 & 0 & \exp\left(-i\frac{\omega}{c} q_{i4} d_i\right) \end{pmatrix} \tag{5.42}$$

Utilizing this matrix, the transfer matrix T_i for each layer is written as following where the matrix contains the parts from the enclosing interface matrices and the propagation matrix,

$$T_i = A_i P_i A_i^{-1} \tag{5.43}$$

Therefore, the total transfer matrix of all *N* layers can be computed by determining

$$T_{tot} = \prod_{i=1}^{N} T_i \tag{5.44}$$

The transfer matrix of the full system, T_N is obtained using the total transfer matrix which contains the propagation as well as interface matrices in order to show the equivalence with the methods observed from the literature,[6, 7, 9, 11]

$$
\begin{aligned}
T_N &= A_0^{-1} T_{tot} A_{N+1} \\
&= A_0^{-1} T_1 T_2 ..... T_N A_{N+1} \\
&= A_0^{-1} A_1 P_1 A_1^{-1} A_2 P_2 A_2^{-1} ... A_N P_N A_N^{-1} A_{N+1} \\
&= L_1 P_1 L_2 P_2 \ ... L_N P_N \ L_{N+1}
\end{aligned}
\tag{5.45}
$$

The first line of eq. (5.45) can easily be implemented in a computer program and it directly shows the computation of the transfer matrix of a single interface which is $T_0 = A_0^{-1} A_1$. The last line describes how the propagation of electromagnetic waves through multilayer structure can be solved by stringing together the interface matrices, $\mathbf{L}_i$ and propagation matrices, P_i in sequence.

In order to calculate the transmitted and reflected coefficients for both *s* and *p*-polarization, the following formula from Yeh[7] is being used

$$
\vec{E}_0^- = T_N \vec{E}_{N+1}^+ \tag{5.46}
$$

where $\vec{E}_{i-1}^-$ and $\vec{E}_i^+$ represent the electric fields on both the sides of the interface which is in between layer *i* -1 and *i*. In order to obtain the coefficients, the T_N needs to be transformed in such a way that the order of the field components is in the following the order:

$$
\vec{E}' = \begin{pmatrix} E_t^p \\ E_r^p \\ E_t^s \\ E_r^s \end{pmatrix}. \tag{5.47}
$$

Therefore, the transformation that is consistent with the formalism of Yeh is,

$$
T_N' = \Omega_{1324}^{-1} T_N \Omega_{1324} \tag{5.48}
$$

where,

$$
\Omega_{1324} = \begin{pmatrix} 1 & 0 & 0 & 0 \\ 0 & 0 & 1 & 0 \\ 0 & 1 & 0 & 0 \\ 0 & 0 & 0 & 1 \end{pmatrix} \tag{5.49}
$$

The components of T_N' are employed to determine the amplitude reflection coefficients: r_{ss} and r_{pp} for *s* and *p*-polarized waves, and r_{ps} and r_{sp} for the mode coupling:

$$r_{pp} = \frac{T'_{21}T'_{33} - T'_{23}T'_{31}}{T'_{11}T'_{33} - T'_{13}T'_{31}} \tag{5.50}$$

$$r_{ss} = \frac{T'_{11}T'_{43} - T'_{41}T'_{13}}{T'_{11}T'_{33} - T'_{13}T'_{31}} \tag{5.51}$$

$$r_{ps} = \frac{T'_{41}T'_{33} - T'_{43}T'_{31}}{T'_{11}T'_{33} - T'_{13}T'_{31}} \tag{5.52}$$

$$r_{sp} = \frac{T'_{11}T'_{23} - T'_{21}T'_{13}}{T'_{11}T'_{33} - T'_{13}T'_{31}} \tag{5.53}$$

Similarly, the amplitude transmission coefficients are[15]:

$$t_{pp} = \frac{T'_{33}}{T'_{11}T'_{33} - T'_{13}T'_{31}} \tag{5.54}$$

$$t_{ss} = \frac{T'_{11}}{T'_{11}T'_{33} - T'_{13}T'_{31}} \tag{5.55}$$

$$t_{ps} = \frac{-T'_{31}}{T'_{11}T'_{33} - T'_{13}T'_{31}} \tag{5.56}$$

$$t_{sp} = \frac{-T'_{13}}{T'_{11}T'_{33} - T'_{13}T'_{31}} \tag{5.57}$$

The intensity reflectivity, *R* and the intensity transmissivity *T* the polarizations are :

$$\text{and} \qquad \begin{aligned} R_{mn} &= \left|r_{mn}\right|^2 \\ T_{mn} &= \left|t_{mn}\right|^2 \end{aligned} \tag{5.58}$$

where the subscripts *m* an *n* correspond polarizations as defined for *r* and *t*. Note that the total transmission of the multilayer structure is distinct from *T* since the energy conservation also needs to be considered. In the following section, the reflectivity and transmittivity of a sample isotropic multilayered structure will be compared with the 4×4 transfer matrix to verify the formalism.

5.3 Fresnel's Equations: Reflection and Transmission for 3-layer Isotropic Media

We will test the 4×4 matrix method by comparing it to the simpler isotropic treatment using Fresnel's equations. This formulation of the Fresnel reflection and transmission coefficients is taken from Born & Wolf and summarized here.[3] The layers in the stack are indexed 1, 2, 3, with the wave incident from layer 1. The angle of propagation to the surface normal in each medium is θ_i. The complex refractive indices of each layer are $\tilde{n}_i$. The thickness of layer 2 is d and the optical path length in layer 2 is β. The wavelength in vacuum λ_0 and d are the only length scales in the problem and must be in the same units. The amplitude reflection and transmission coefficients for the stack are r_m and t_m, respectively, for TE and TM polarized modes as indicated by the subscripts. The corresponding power reflection and transmission coefficients for each mode are R_m and T_m, respectively. The amplitude reflection and transmission coefficients for each interface in the stack are indexed in the order traversed by the incident wave, j and k, and the mode m. Thus r_{12}^{TE} and t_{12}^{TE} are the amplitude reflection and transmission coefficients for the interface between layers 1 and 2 for the TE polarized mode. Note the power transmission coefficients are not simply the modulus of the amplitude squared. This is because the magnitudes of the electric and magnetic fields inside each medium, for the same intensity, depend on the refractive index. The transmission coefficients compare the fields between two different media, where the reflection coefficients compare the field in the same medium. The pre-factors are required to account for the different magnitudes.

$$
\begin{aligned}
&p_i = \tilde{n}_i \cos\theta_i\,; \quad q_i = \frac{1}{\tilde{n}_i}\cos\theta_i\,; \quad \theta_i = \sin^{-1}\left(\frac{\tilde{n}_1}{\tilde{n}_i}\sin\theta_1\right); \quad \beta = \frac{2\pi}{\lambda_0}\tilde{n}_2 d\cos\theta_2 \\
&r_{jk}^{TE} = \frac{p_1 - p_2}{p_1 + p_2}; \quad t_{jk}^{TE} = \frac{2p_1}{p_1 + p_2} \\
&r_{jk}^{TM} = \frac{q_1 - q_2}{q_1 + q_2}; \quad t_{jk}^{TM} = \frac{2q_1}{q_1 + q_2} \\
&r_m = \frac{r_{12}^m + r_{23}^m \exp(2i\beta)}{1 + r_{12}^m r_{23}^m \exp(2i\beta)}; \quad t_m = \frac{t_{12}^m t_{23}^m \exp(2i\beta)}{1 + r_{12}^m r_{23}^m \exp(2i\beta)} \\
&R_{TE} = \left|r_{TE}^2\right|; \quad R_{TM} = \left|r_{TM}^2\right|; \quad T_{TE} = \frac{p_3}{p_1}\left|t_{TE}^2\right|; \quad T_{TM} = \frac{q_3}{q_1}\left|t_{TM}^2\right|
\end{aligned}
\tag{5.59}
$$

For non-absorbing media, eqs. (5.59) must satisfy the law of conservation of energy such that, $R_m + T_m = 1$. In the case of normal incidence ($\theta_1 = 0$), there is no distinction between TE and TM polarization and we drop the subscripts. The amplitude and power reflection coefficients for this special case simplify to:

$$
\begin{aligned}
&r = \frac{n_1 - n_2}{n_1 + n_2}; \quad t = \frac{2n_1}{n_1 + n_2} \\
&R = \left(\frac{n_1 - n_2}{n_1 + n_2}\right)^2; \quad T = \left(\frac{2n_1}{n_1 + n_2}\right)^2
\end{aligned}
\quad . \tag{5.60}
$$

5.4 Testing of 4×4 Transfer Matrix for the Isotropic Case

The transfer matrix formalism presented by Passler and Parrmann[12] are applicable to any number of layers and any wavelength where each layer would be presented by an arbitrary dielectric tensor. To test the generality of this formalism, a direct comparison with isotropic formalism is discussed in this section.

Since, the Fresnel coefficients for reflection are dependent on the angle of incidence and if a plane wave with a mixture of TE and TM waves is incident at a dielectric interface at a particular angle of incidence where the reflected radiation gets linearly polarized with the electric field vector perpendicular to the incident plane (Brewster's angle). Their r_p vanishes and the *p*-polarized incident wave is completely transmitted at this certain angle of incidence,

$$\theta_B = \tan^{-1}\left(\frac{n_2}{n_1}\right) \tag{5.61}$$

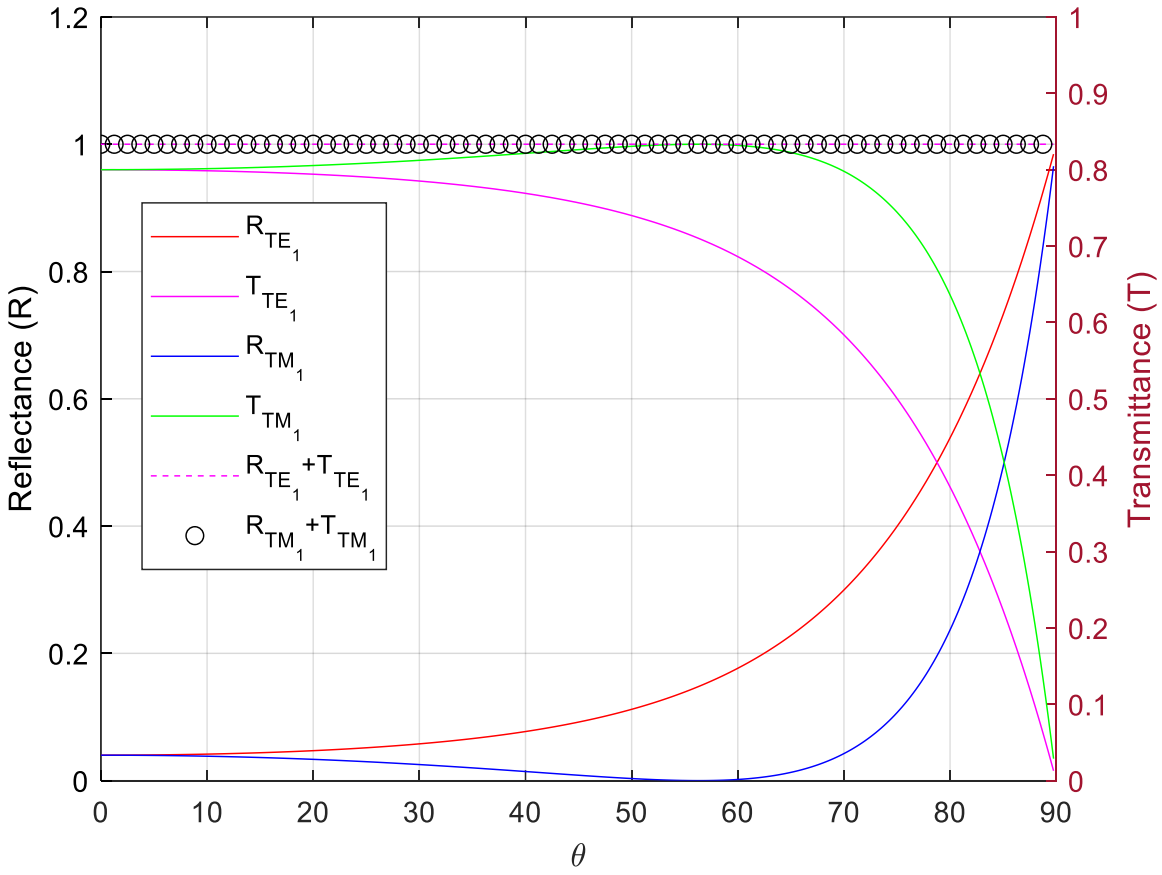

Figure 5.2: Comparison between the reflectance and transmittance of TE and TM modes for 3-layer system (air-air-glass).

In order to verify our method for three layered media with the Fresnel formulas, it is compared with different setups consisting typical glass (n = 1.5) and air (n = 1). The angle of incidence started from 0° to 90°. The power reflectance should be 4% at the normal incidence according to eq. (5.60) and in Figure. 5.2, 5.3, 5.4 and 5.5, it is shown that the reflectance for TE modes at normal incidence is also 4%. The Brewster's angle from air to glass is at 56˚ and for both Figure. 5.2 and 5.3, θ_B is at 56˚. Their critical angles for glass to air is at 41.81˚ and that

verifies in the Figure 5.4 and 5.5, also. Similarly, Brewster's angle is 56˚ for TM modes at normal incidence as well and all of them satisfy, $R_m + T_m = 1$.

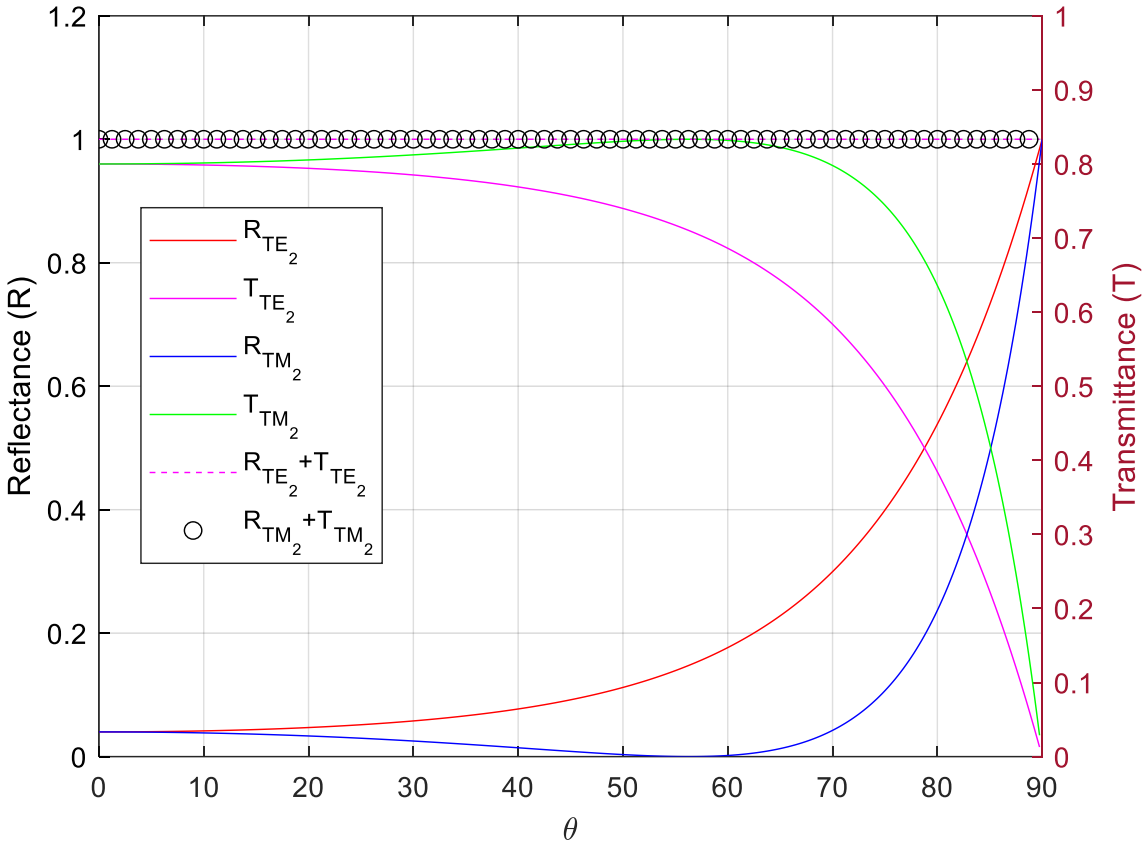

Figure 5.3: Comparison between the reflectance and transmittance of TE and TM modes for 3-layer system (air-glass-glass).

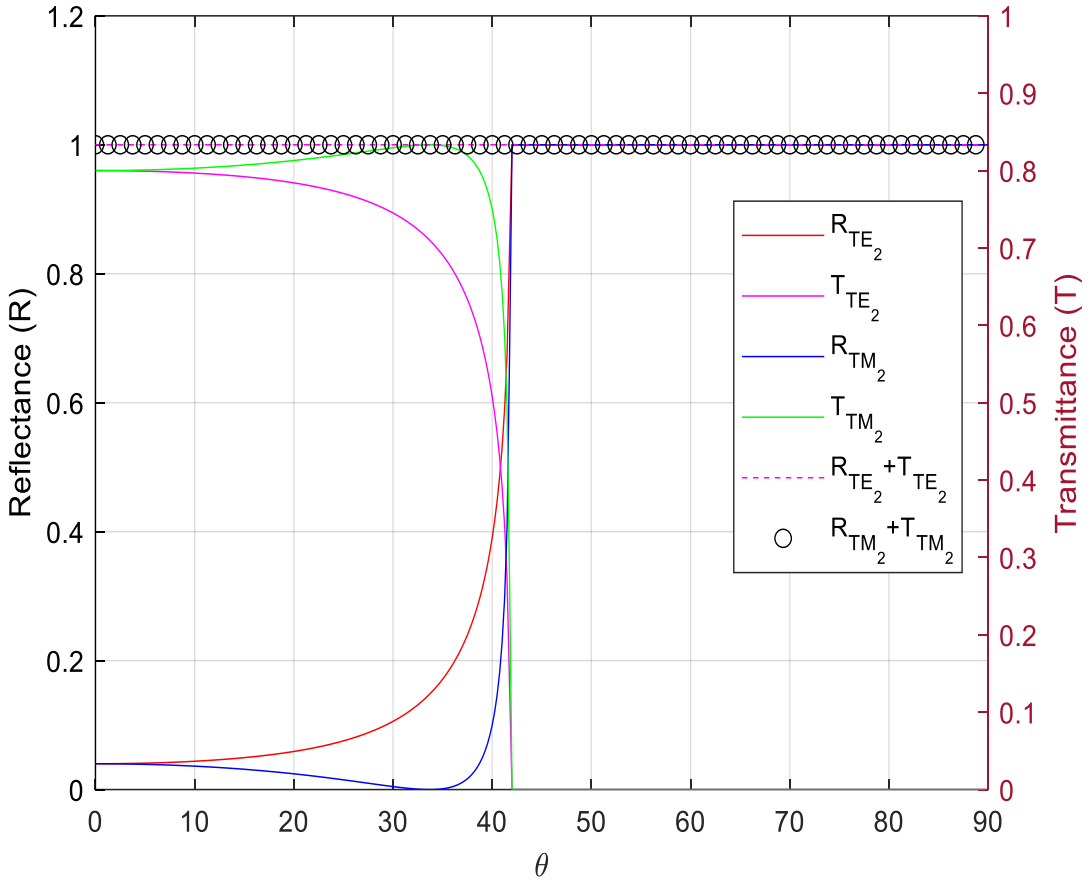

Figure 5.4: Comparison between the reflectance and transmittance of TE and TM modes for 3-layer system (glass-air-air).

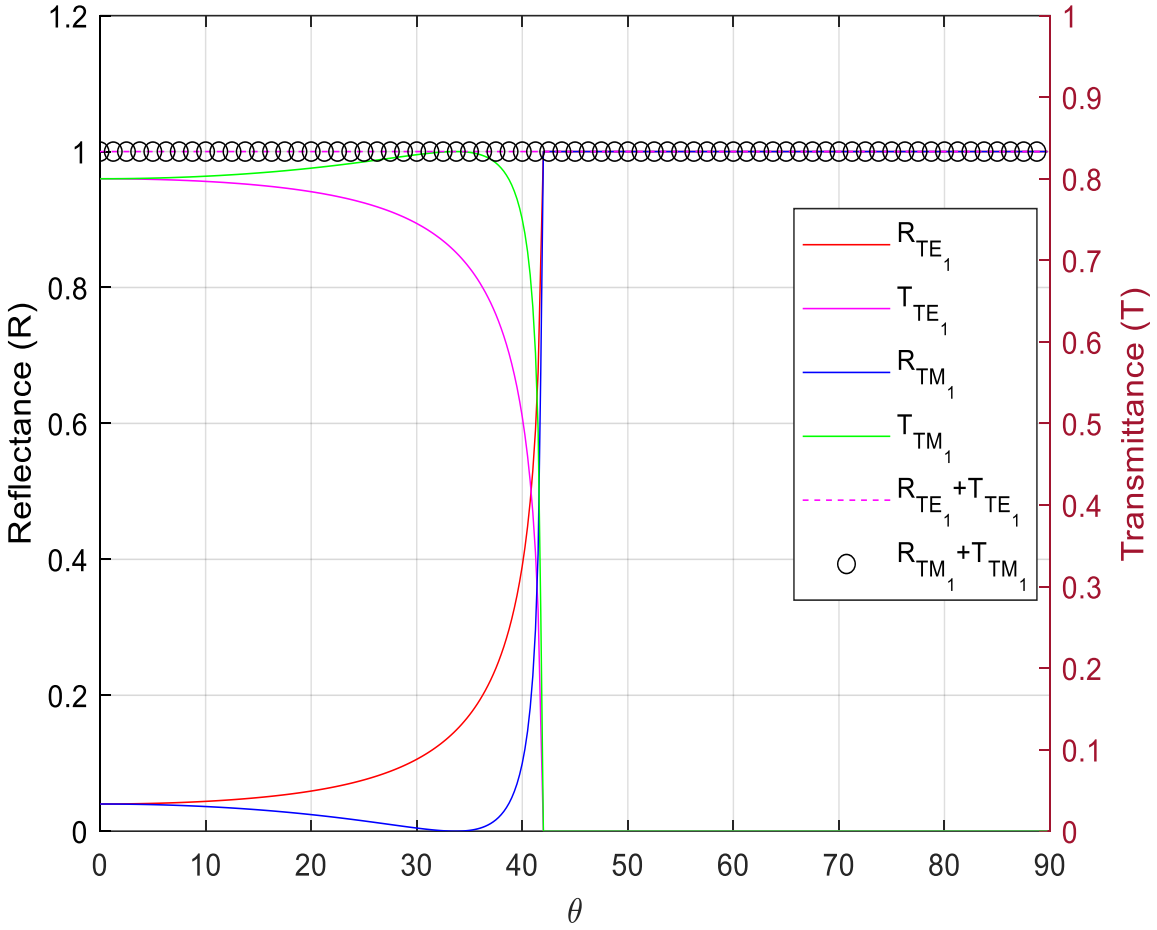

Figure 5.5: Comparison between the reflectance and transmittance of TE and TM modes for 3-layer system (glass-glass-air).

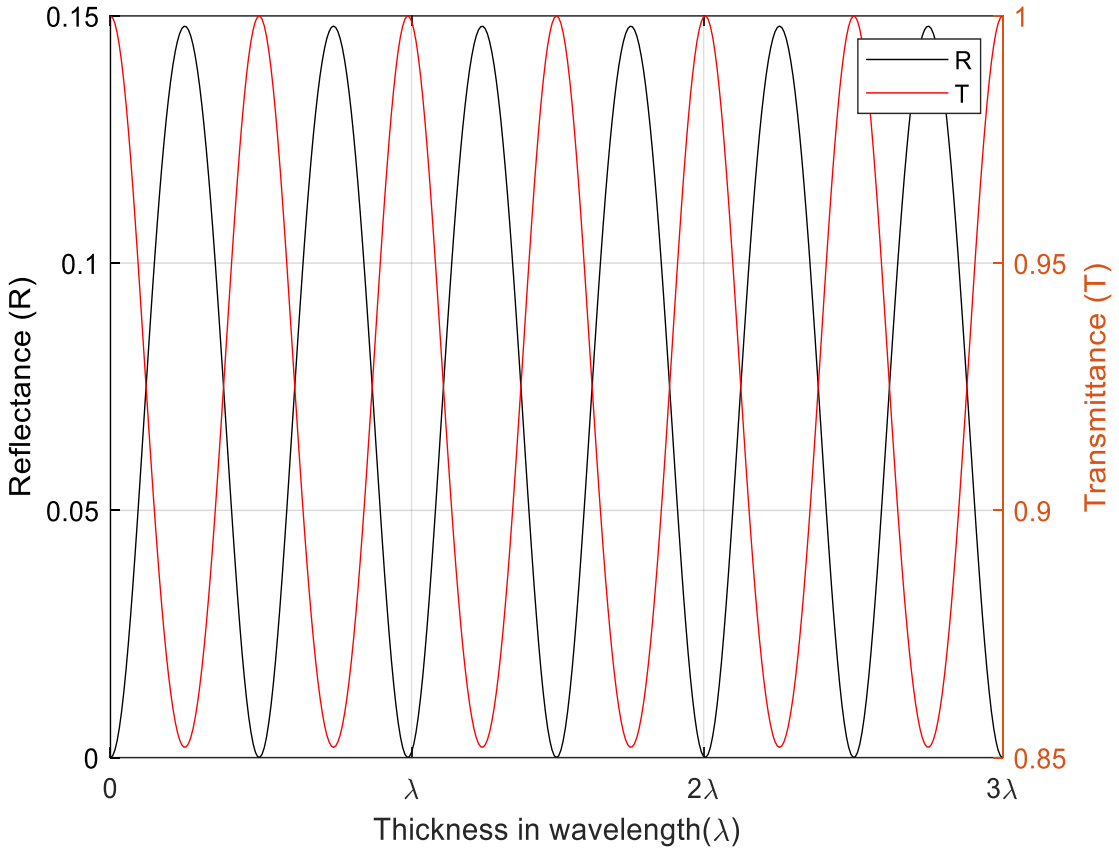

Figure 5.6: Comparison of *R* and *T* over varying thickness in the unit of wavelength for air-glass-air where the thickness of glass and the wavelength is 1.0 μm.

In order to verify the interference for the case of air-glass-air and glass-air-glass, we let the optical thickness of layer 2 vary from 0 to 2 wavelengths at normal incidence. From Figure 5.6 and 5.7, it is demonstrated that *R* and *T* oscillate in thickness with a period of half the wavelength in layer 2 and at zero thickness, $R = 0$ and $T = 1$. When layer 2 is air in Figure 5.7, there are two complete oscillation, whereas in Figure 5.6, when layer 2 is glass, the number of oscillation increases from two to three. Therefore, with increasing thickness of layer 2, the number of oscillations also increases. This satisfies $R_m + T_m = 1$ also.

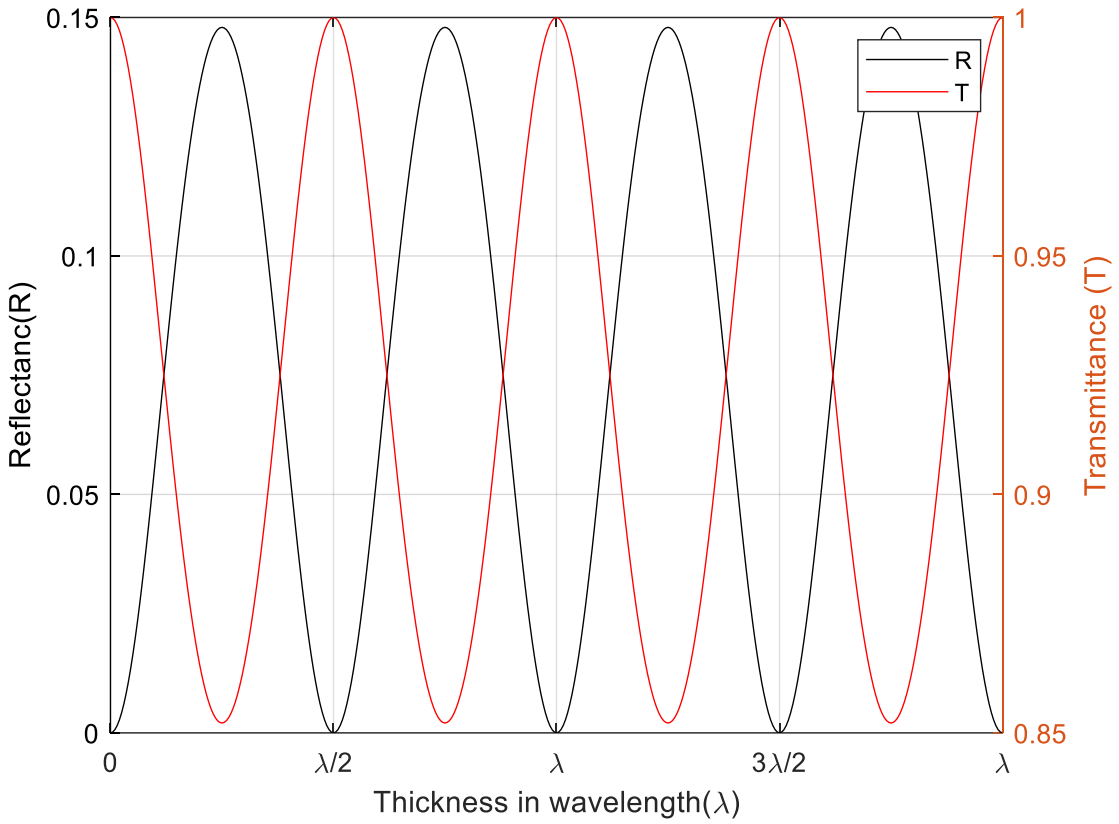

Figure 5.7: Comparison of *R* and *T* over varying thickness in the unit of wavelength for glass-air-glass where the wavelength is 1.0 μm.

Next, to test the 4×4 matrix formalism by Passler and Parrmann, we calculated the reflection using the Fresnel's formula and compared both of them.[12, 15] The calculation of reflectivity of Au in the mid-IR will be very relevant in this case. In order to do that, reflectance of both the TE and TM waves, e.g., R_{TE} and R_{TM} are measured from a structure of three layer consisting air-air-gold at an incident angle of 30˚ and compared them with the reflectance from both the polarizations e.g., R_{TEp} and R_{TMp} which are calculated using 4×4 matrix formalism.

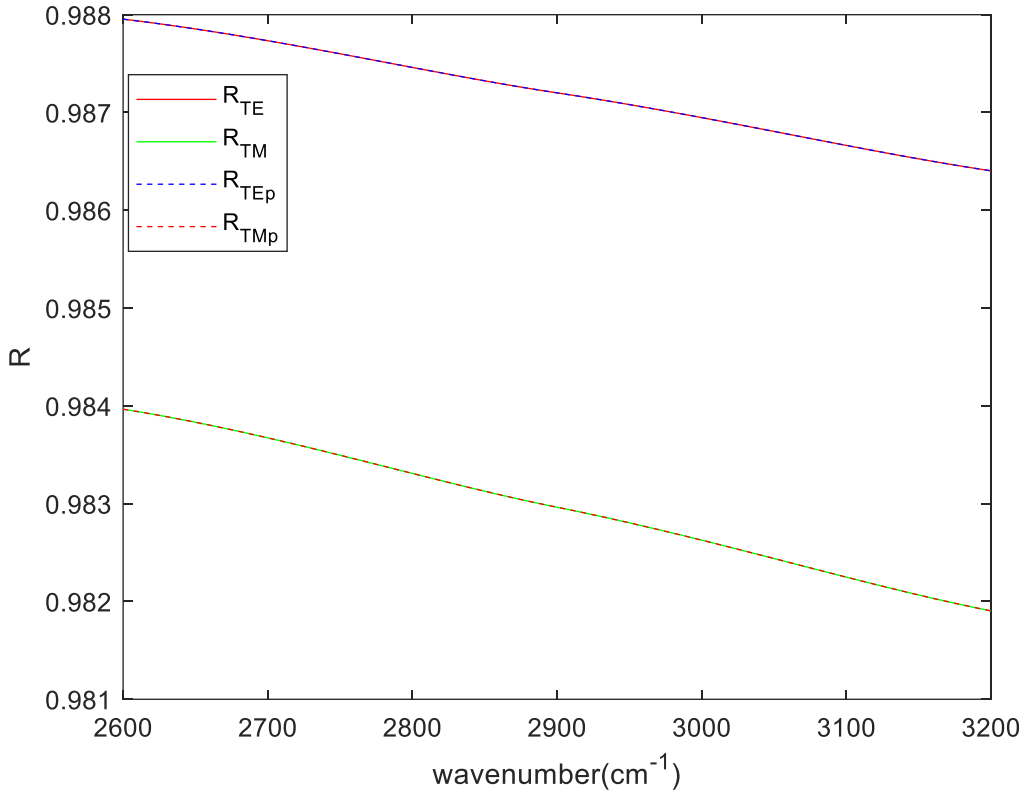

Figure 5.8: Comparison of the reflectance between R_{TE}, R_{TM} calculated from Fresnel's equation and R_{TEp}, R_{TMp} from 4x4 matrix formalism from Passler and Parrmann for air-air-gold.

For these isotropic test cases, we showed that the 4×4 matrix formalism is in good agreement with the simpler Fresnel's formulas for reflectance and transmittance of three layer media. In following chapter, few anisotropic structural media will be measured and compared with the theoretical method.

5.5 References

1. Jones, R. C., A New Calculus for the Treatment of Optical Systems I. Description and Discussion of the Calculus. *J. Opt. Soc. Am* **1941,** *31* (7), 488-493.
2. Abelès, F., Recherches sur la propagation des ondes électromagnétiques sinusoïdales dans les milieux stratifiés. *Ann. Phys. (Paris)* **1950,** *12* (5), 596-640.
3. Born, M.; Wolf, E., *Principles of Optics Electromagnetic Theory of Propagation, Interference and Diffraction of Light*. 1980.

4. Teitler, S.; Henvis, B. W., Refraction in Stratified, Anisotropic Media. *J. Opt. Soc. Am* **1970,** *60* (6), 830-834.
5. Holmes, D. A.; Feucht, D. L., Electromagnetic Wave Propagation in Birefringent Multilayers. *J. Opt. Soc. Am* **1966,** *56* (12), 1763-1769.
6. Yeh, P., Electromagnetic propagation in birefringent layered media. *J. Opt. Soc. Am* **1979,** *69* (5), 742-756.
7. Yeh, P., Optics of anisotropic layered media: A new 4 × 4 matrix algebra. *Surf. Sci.* **1980,** *96* (1), 41-53.
8. Yeh, P.; Hendry, M., Optical Waves in Layered Media. *Phys. Today* **1990,** *43* (1), 77-78.
9. Berreman, D. W., Optics in Stratified and Anisotropic Media: 4×4-Matrix Formulation. *J. Opt. Soc. Am* **1972,** *62* (4), 502-510.
10. Parikh, A. N.; Allara, D. L., Quantitative determination of molecular structure in multilayered thin films of biaxial and lower symmetry from photon spectroscopies. I. Reflection infrared vibrational spectroscopy. *J. Chem. Phys.* **1992,** *96* (2), 927-945.
11. Xu, W.; Wood, L. T.; Golding, T. D., Optical degeneracies in anisotropic layered media: Treatment of singularities in a 4×4 matrix formalism. *Physical Review B* **2000,** *61* (3), 1740-1743.
12. Passler, N. C.; Paarmann, A., Generalized 4 × 4 matrix formalism for light propagation in anisotropic stratified media: study of surface phonon polaritons in polar dielectric heterostructures. *Opt. Soc. Am. B* **2017,** *34* (10), 2128-2139.
13. Drude, P., *The theory of optics*. England: Longmans, Green, and Co.: England, 1902.
14. Li, Z.-M.; Sullivan, B. T.; Parsons, R. R., Use of the 4 × 4 matrix method in the optics of multilayer magnetooptic recording media. *Appl. Opt.* **1988,** *27* (7), 1334-1338.
15. Passler, N. C.; Paarmann, A., Generalized 4 × 4 matrix formalism for light propagation in anisotropic stratified media: study of surface phonon polaritons in polar dielectric heterostructures: erratum. *J. Opt. Soc. Am. B* **2019,** *36* (11), 3246-3248.

Chapter 6

Infrared Reflection Absorption Spectroscopy (IRRAS) Simulated from Molecular Dynamics (MD) Models

In this chapter, the primary focus is to bridge the theoretical approaches with the experimental technique and therefore the IRRAS spectra is being simulated using the molecular dynamics (MD) models. In order to simulate IRRAS from MD models, it is important to understand the basic principal and the underlying theory of interaction of photons with the thin films and surfaces. So first in this chapter, we start with the basis on which IRRAS is developed, then the strategies required to simulate the spectra from the MD models followed by the practical approaches to obtain reflectivity and transmittivity from experimental spectrum of anisotropic multilayer structure.

6.1 Basic Theory of IRRAS

IRRAS is specifically useful optical tool to study thin films such as SAMs adsorbed on reflective noble materials e.g. gold. It provides the most definitive means of identifying the molecular groups of the thin film as well as their orientation with respect to the surface of gold. Experimentally, it measures absorption spectra of the substrate in the MIR region which arise due to the bond stretching and bending of molecules. On the metal substrate, the vibrational modes of adsorbates are subject to the selection rule which states that the vibrational modes which give rise to an oscillating dipole perpendicular to the surface can be detected as active IR mode. This system follows this selection because when the system has a metal substrate, the transition dipole of a bond forms a quadrupole with the image dipole and the tangential components gets suppressed due to image charges. Hence, the transition dipole of the bond forms a stronger dipole with the image dipole and the perpendicular components become enhanced. The best sensitivity of IRRAS on metal is achieved when the IR light is incident at a grazing angle. Next, the absorption causes dispersion in refractive index and it also changes the reflectivity close to the absorption region. This change causes the effect of shifting the apparent

absorption. These electromagnetic effects are taken into account by Fresnel's equation and by the 4×4 transfer matrix methods.[1, 2]

6.2 Quantitative Analysis of Spectroscopic Intensities

To understand the process of interaction with a stack of film in terms of a standing wave propagating through the entire structure while the incoming beam is dividing some of its intensity between reflection and transmission at each interface, a system with three layer stack is demonstrated.

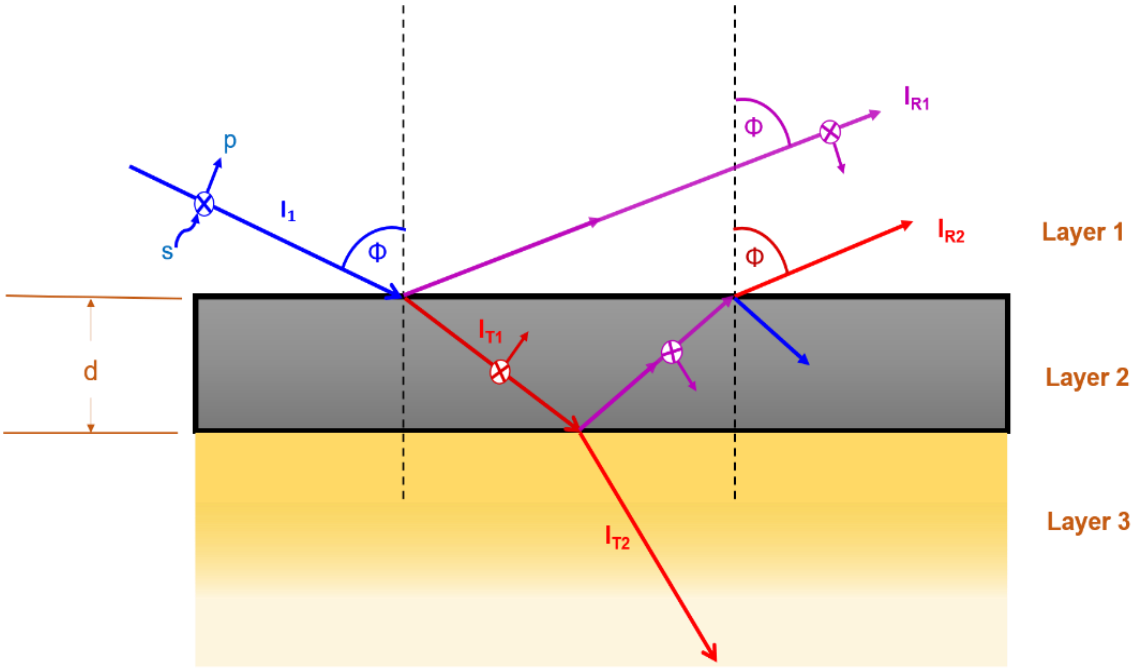

Figure 6.1: Schematic diagram of a plane wave impinging on a planar film at an angle of incidence, φ and thickness of film is d. The structure consists of layer of ambient medium (1), a top layer (2, grey) and an infinite layer (3, yellow)

The illustrated multilayered system consists of N semi-infinite, parallel, planar slabs with a thickness of t_N for each layer and the general reflection and transmission experiment will be discussed considering this system. The slab surface is chosen to be in the *xy*-plane and the *xz*-plane contains the plane of incidence. Therefore, the incoming beam can be rotated at any direction around the *xy*-plane and along that direction, the plane of incidence can be rotated

azimuthally at an angle φ from the *x*-axis. The direction of the electric field vector of the incident beam with respect to the plane of incidence defines the state of polarization of the beam. A fraction of the incident beam is transmitted through the sample and, if the layers of the sample are transparent sufficiently to the radiation, then some part of the initial beam leaves the last layer and transmits into an infinite, adjacent medium. The remaining fraction of the incident beam is reflected from the planar surface. Since, pure *s* and *p*-polarized incident beam usually interact differently with the sample, and hence for an elliptically polarized incident light consisting both *s* and *p*-elements, the polarization will be altered upon leaving the sample.

A light beam with an intensity I_1 propagating through non-absorbing medium 1 which is generally air or vacuum, impinges at the interface between media 1 and 2 at an angle of incidence φ. A reflected specular beam with an intensity I_{R1} is generated which returns to medium 1 with the same angle φ and a beam is also refracted with an intensity I_{T1} into medium 2. This refracted transmitted beam will continue to go through the sample and leave from the other side of the last layer of the sample if both media 2 and 3 are appropriately non-absorbing enough. The incident beam which is getting reflected and transmitted within the phase boundaries at the interfaces generates constructive and destructive interferences of the electric fields and absorption is also produced due to excitation of quantum states. Together they regulate the total intensity of the output beam of light.

In order to regulate the spectral computation, the most thorough and meticulous approach so far is the 4×4 transfer matrix method formalism. In this method, the electric and magnetic field vectors at any depth in the sample are calculated by obtaining relative values at the outer interfaces of the sample. This can be achieved by operating a sequential matrix operation across each interface. This matrix formalism has been discussed rigorously in the previous chapter. Now, we are going to employ this method to simulate IRRAS from molecular dynamics model.

6.3 Testing

Since multiple modes of excitations reside in the same spectral region, polyatomic molecular spectra become complicated and it may cause overlapping bands. In the mid-IR region, stretching vibrations of C-H bonds become complicated due to the overlapping of methyl and methylene absorption mode. Along with the overlapped modes, a broad Fermi resonance

peaks with the overtones of lower frequency modes are also superimposed.[3] The envelope of the absorption of spectra is constructed basically by taking a direct sum of the intensities which are contributing to the absorption line, i.e., $\sum_{i=j}^{n} k_i(\omega)$ where $k_i(\omega)$ is the k starting from the ith excitation mode in the jth frequency interval which is centered at the frequency ω_j.

In order to test our model, we calculated the IRRAS spectra of a *n*-decanethiol ($C_{10}H_{22}S$) molecular chain. The laboratory coordinate system is chosen to have the backbone of the molecular chain along *z*-axis and the alkyl tilt chain in the *xz*-plane. Later, the molecular coordinates of each transition dipole moments are transformed into the surface frame by applying the proper rotation matrix (discussed in chapter 4). The C–H stretching modes for *n*-decanethiol, the anisotropic *k* per mode and the direction of the transition dipole moments associated with the fundamental vibrational modes are extracted from Parikh and Allara.[4] The assignments of the modes and along with the peak shape are listed in Table 6.1. Using the analytic pair function of Lorentzian and Gaussian line shape (discussed in chapter 3), Δn tensor per mode were calculated from the anisotropic *k* tensor per mode. Then, the Δn tensor and *k* tensor were rotated back to the surface frame and were diagonalized to obtain the principal values Δn and *k.* A comparison between them is demonstrated in Figure. 6.2.

Table 6.1: Assignment of the frequencies of the maximum value of *k* per C-H stretching mode absorptions of *n*-Decanethiol.[4]

Peak Frequency (cm^{-1})	FWHM (cm^{-1})	L Fraction	Description of mode	Anisotropic k per mode
2850	9.21	0.229	CH_2 sym. str. d+	0.332
2853	9.21	0.898	Alpha-CH_2 sym. str. d_a+	0.0694
2862	9.54	0.843	Beta- CH_2 sym. str. d_b+	0.0492
2879	11.2	0.665	CH_3 sym. str. r+	0.0541
2895	14.5	0.868	FR of CH_2 sym. str. d_{FR}+	0.00521
2907	11.2	0.842	FR of CH_2 sym. str. d_{FR}+	0.00521
2918	11.2	0.446	CH_2 asym. str. d−	0.0578
2925	12.5	0.709	Alpha-CH_2 asym. str. d_a−	0.216
2935	10.5	0.653	FR of CH_3 sym. str. r_{FR}+	0.0295
2954	7.89	0.565	CH_3 asym. str. op. r_{op}−	0.0738
2964	13.8	0.611	CH_3 asym. str. ip. r_{ip}−	0.0885

FWHM = Full width at half maxima obtained from the measured band resolution.

sym. = symmetric,

asym. = asymmetric

str. = stretching

FR = Fermi resonance

op. = out of plane

ip. = in plane.

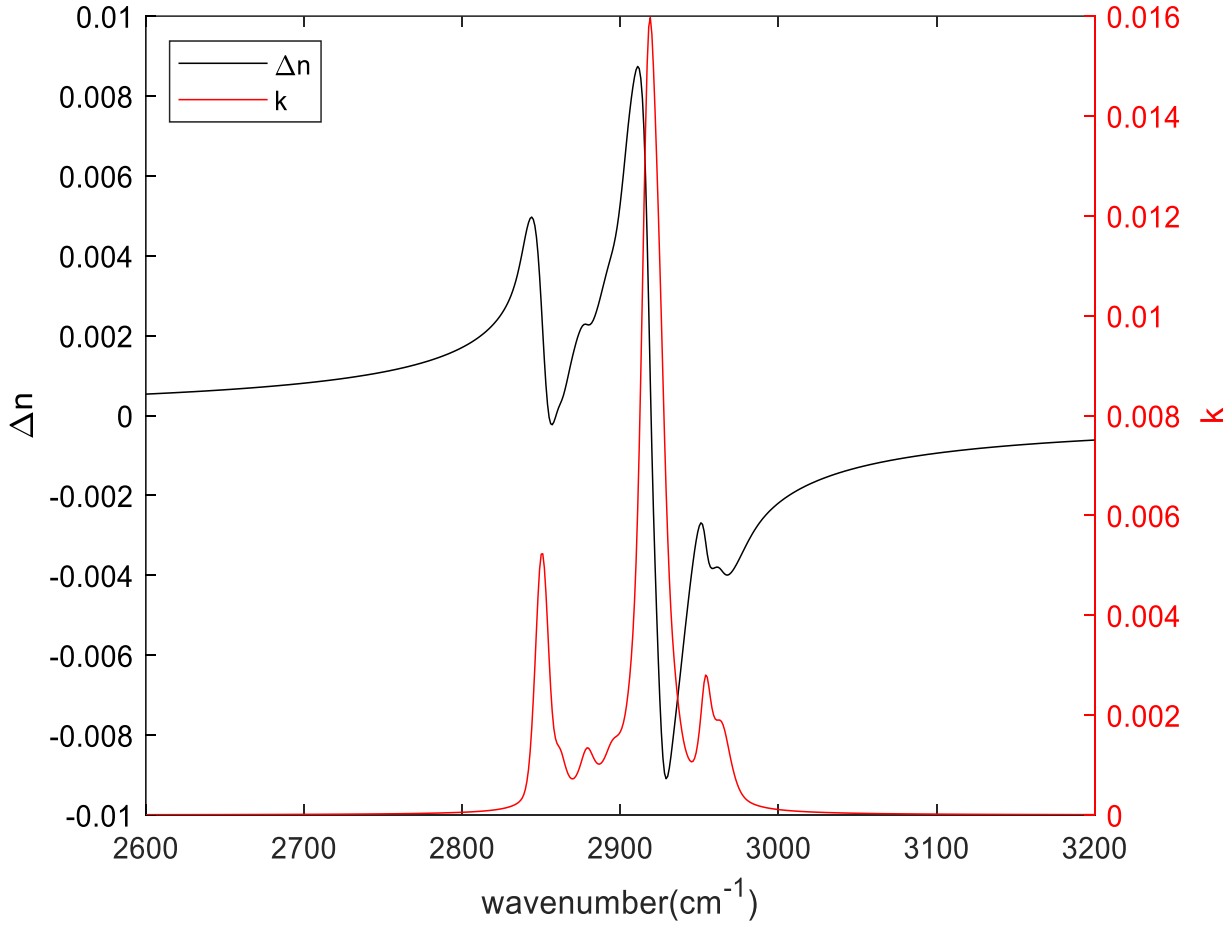

Figure 6.2: A sample plot of *k* and the calculated Δ*n* from *k* of *n*-decanethiol ($C_{10}H_{22}S$) SAM from Table. 6.1.

Next, the high frequency refractive index tensor, n_∞, is calculated by applying the method discussed in chapter 4 using the bond polarizabilities, bond lengths and angles from the literature.[5, 6] And we obtain the complex refractive index tensor, *n* for the thin film. Afterwards, *n* is transformed back into the principal coordinates of n_∞ by applying the rotation matrix which was used previously to calculate n_∞. The principal values of the real part of *n* are defined as n_α, n_β and n_γ where α, β and γ refers to the principal axes of n_∞ and the convention they follow is as $n_\alpha < n_\beta < n_\gamma$..The calculated principal values are listed in Table 6.2.

Table 6.2: The calculated principal values of n_∞ for *n*-decanethiol SAM.

n_α	n_β	n_γ
1.5321	1.5391	1.5768

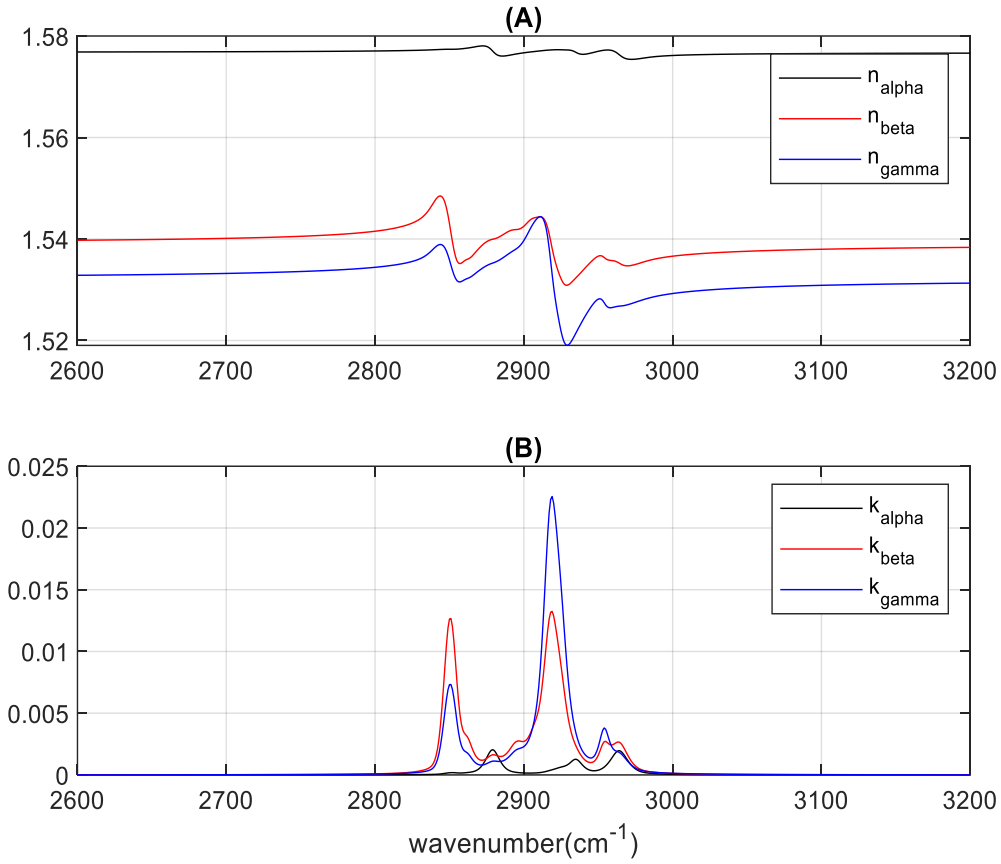

Figure 6.3: *n* and *k* of *n*-decanethiol SAM. (A) Comparison between the principal values of *n* and (B) comparison between the principal values of *k*.

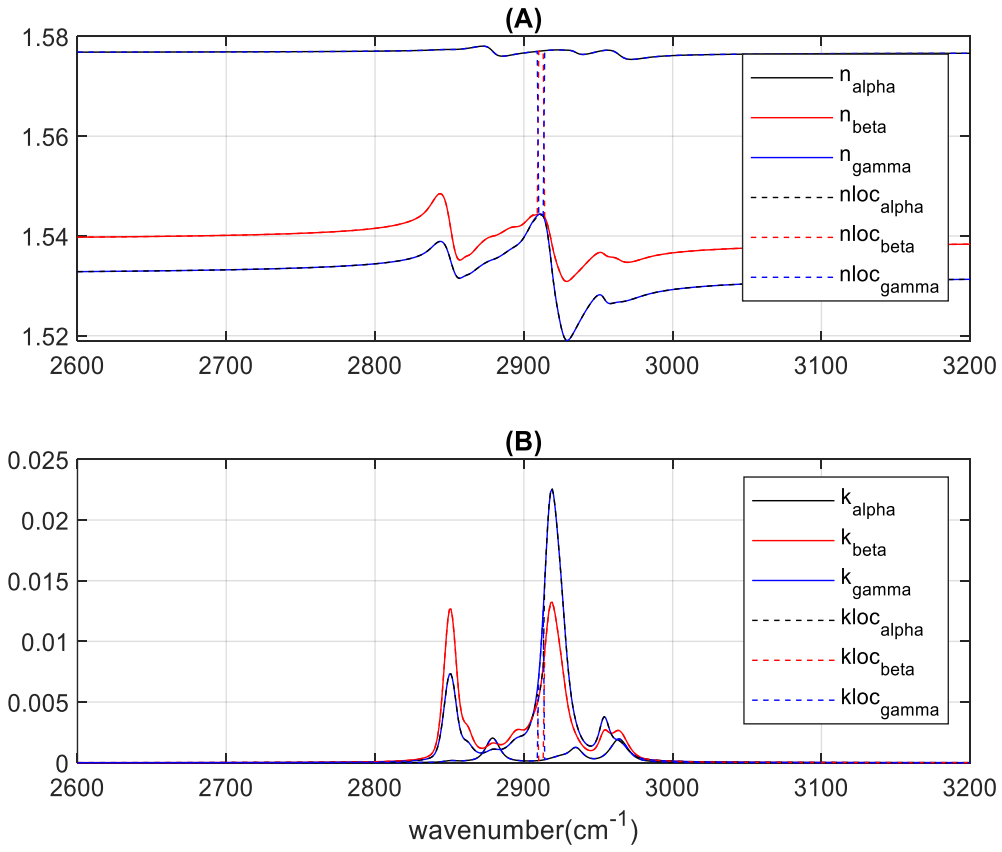

Figure 6.4: *n* and *k* of *n*-decanethiol SAM. (A) Comparison between the principal values of *n* and n_{loc}, diagonalized *n* at each wavelength and (B) comparison between the principal values of *k* and k_{loc}, diagonalized *k* at each wavelength.

The problem that we encountered while diagonalizing *n* of the anisotropic system is that the total complex refractive index tensor cannot be diagonalized because the real and imaginary parts of the complex refractive index have different principal axes and cannot be simultaneously diagonalized. But it is close enough to the principal axes of n_∞ as n_∞ has the largest contribution to the total refractive index, *n*. This hypothesis is tested in Figure 6.4 by diagonalizing *n* at each wavelength. The plots are indistinguishable. Therefore, we choose to pick the fixed reference frame of n_∞ which relates directly to the alignment of the molecular chain and our method of calculating the rotation matrix as well as the diagonalization is viable. The issue regarding the diagonalization requires further investigation and because of that we could only determine the isotropic model of IRRAS of the *n*-decanethiol ($C_{10}H_{22}S$) SAM from MD simulations.

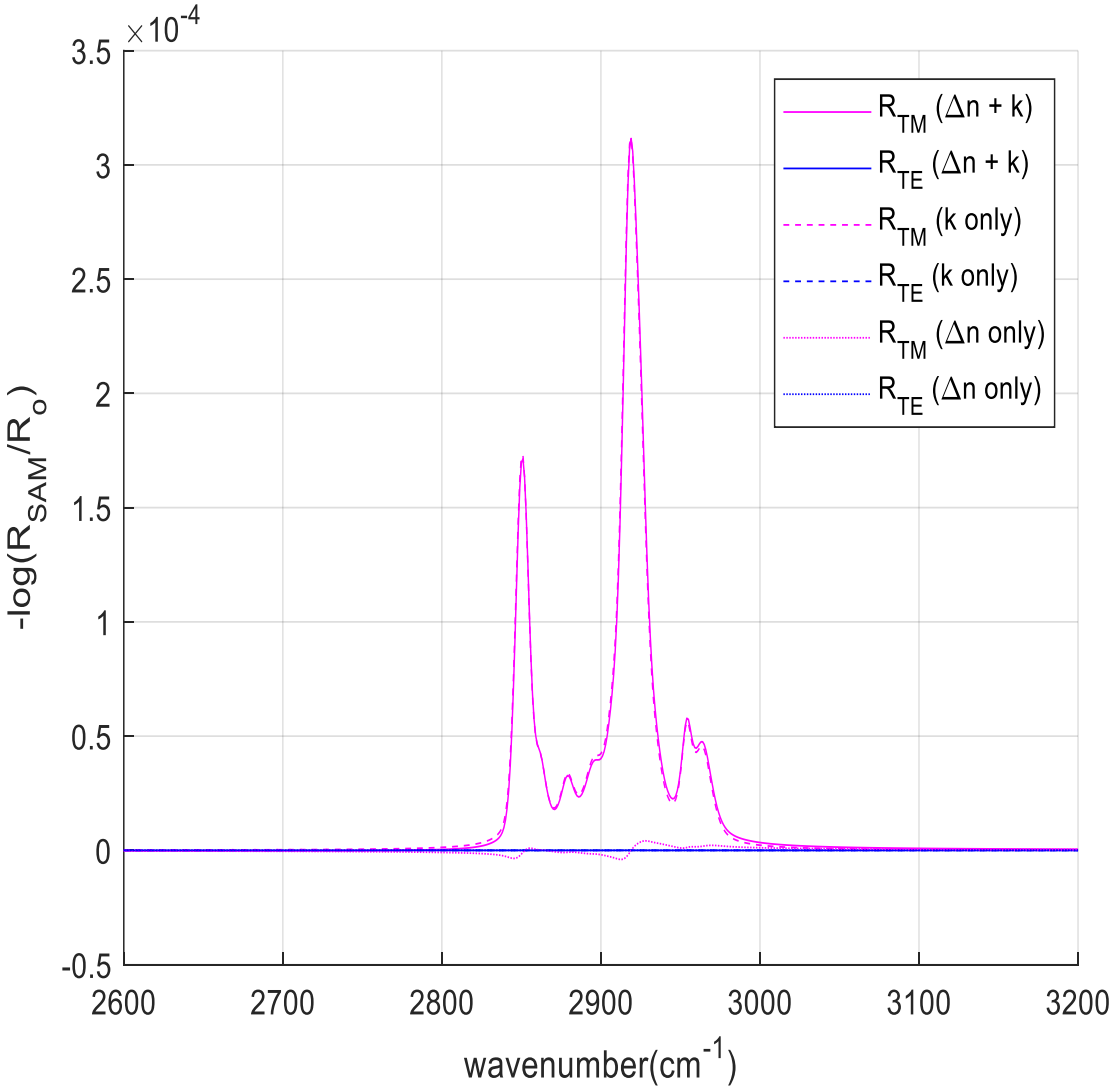

Figure 6.5: Comparison between the reflectance obtained for TE and TM mode using different combinations of Δn and k for the isotropic model of IRRAS for *n*-decanethiol

Since, the complex refractive index tensor, *n* cannot be diagonalized, the attempt of taking the square of the complex principal components of *n* and rotating it back to the reference frame in order to calculate the complex dielectric constant was unsuccessful. The computation of complex dielectric constant resulted in negative imaginary parts in the regions with strong absorption. This result is obviously unphysical and causes the 4×4 transfer matrix method to yield unreasonable results. In Figure 6.5, the isotropic dielectric constant is calculated from the

complex refractive index tensor. The real and imaginary parts are separately diagonalized at each wavelength and then the rms averages are combined in order to construct the average complex refractive index, i.e., the isotropic complex refractive index. This refractive index is next squared in order to compute the isotropic complex dielectric constant at that wavelength.

In future work, we plan to further investigate this issue of diagonalizing the complex refractive index and dielectric tensor by pursuing a slightly different approach to construct the complex polarizability tensor. Then in order to calculate the complex dielectric constant, we plan to adapt the approach of Vuks.[7]

6.4 Reference

1. Passler, N. C.; Paarmann, A., Generalized 4 × 4 matrix formalism for light propagation in anisotropic stratified media: study of surface phonon polaritons in polar dielectric heterostructures. *Opt. Soc. Am. B* **2017,** *34* (10), 2128-2139.
2. Passler, N. C.; Paarmann, A., Generalized 4 × 4 matrix formalism for light propagation in anisotropic stratified media: study of surface phonon polaritons in polar dielectric heterostructures: erratum. *J. Opt. Soc. Am. B* **2019,** *36* (11), 3246-3248.
3. Snyder, R. G.; Hsu, S. L.; Krimm, S., Vibrational spectra in the C・H stretching region and the structure of the polymethylene chain. *Spectrochim. Acta A* **1978,** *34* (4), 395-406.
4. Parikh, A. N.; Allara, D. L., Quantitative determination of molecular structure in multilayered thin films of biaxial and lower symmetry from photon spectroscopies. I. Reflection infrared vibrational spectroscopy. *J. Chem. Phys.* **1992,** *96* (2), 927-945.
5. De Jong, S., Groeneweg, F.; Van Voorst Vader, F., Calculation of the refractive indices of molecular crystals. *J. Appl. Crystallogr.* **1991,** *24* (2), 171-174.
6. Teare, P., The crystal structure of orthorhombic hexatriacontane, $C_{36}H_{74}$. *Acta Cryst.* **1959,** *12* (4), 294-300.
7. Vuks, M. F., Determination of the Optical Anisotropy of Aromatic Molecules from the Double Refraction of Crystals. *Opt. Spectrosc.* **1966,** *20*, 361.

Chapter 7
Conclusion

The motivation of our study is to establish a full anisotropic treatment for simulating the IRRAS of SAMs from all-atom MD simulations and construct a technique to bridge the result from the simulation to the experimental measurements. In the effort to understand the detailed structure of SAMs, a full anisotropic model is described in this study to simulate IRRAS spectra in mid-IR which is based on the work done by Parikh and Allara.[1]

To fully harness the useful information from the IRRAS spectra in MIR, a complex refractive index tensor is needed to be calculated in mid-IR. The refractive index tensor can be described as a sum of the partial molar refraction tensor of each component. In our case, the sum of the atomic bond polarizabilities is used to calculate the high frequency refractive index tensor, n_∞ and a sum of different modes of absorptions is employed calculated the complex refractive index tensor in MIR, Δn.

Kramers–Kronig (K-K) transformation pairs find the contribution of refractive index by the absorption from IR active modes. Since the numeric K-K integration is computationally expensive, we established analytic function pairs using the Gaussian and Lorentzian line shapes. The K-K transform analytic function pairs for Gaussian and Lorentzian absorption profiles match the result from numeric K-K integration. The error which we encountered in this process was due to the artifacts that occur when the integration range is truncated. We verified that this error goes away and converges to zero as we increase range point density of the integration. This analytic function as K-K transformation pairs are computationally less expensive and can easily be used instead of K-K transformation pairs.

In order to calculate the high frequency refractive index tensor, first the bond polarizabilities need to be employed to calculate the molecular polarizability tensor. Then the polarizability tensor is rotated into the coordinate frame that diagonalizes it and the refractive index tensor is calculated. Next, the refractive index tensor is rotated back again into the unit cell coordinate frame. We tested our model for *n*-hexatriacontane ($C_{36}H_{74}$). The anisotropic principal refractive indices, n_α, n_β, and n_γ are calculated using the crystal structure from the literature and they are in good agreement with the experimental measurements.[2]

To calculate the reflectance and transmittance of the anisotropic material, we used the 4×4 matrix formalism by Passler and Paarmann.[3, 4] To verify the 4×4 matrix formalism, we tested their method for some special cases with Fresnel's formalism for 3-layer system. The results for Brewster's angle and critical angle from both the formalisms are same and they match. Another test is conducted for the interference with varying thickness and it verifies that R and T oscillate in thickness with a period of half the wavelength in the 2nd layer. Therefore, the 4×4 matrix formalism is viable to employ in the calculation of the simulation of IRRAS spectra.

Next, the model from our study to simulate the IRRAS spectra is verified by computing the IRRAS spectrum of *n*-decanethiol ($C_{10}H_{22}S$) on gold substrate. The IR active modes were measured from the MD simulations. The complex refractive index tensor was calculated by determining n_∞, Δn and k. The complex refractive index and dielectric tensor cannot be diagonalized using this method because the real and imaginary parts of them have different principal axes. This is planned to be investigated in our future work. The isotropic model of IRRAS spectra for both TE and TM modes are calculated using the 4×4 matrix formalism for different combinations of Δn and k and it helps us to understand the contribution of each of the properties. We wanted to understand if there are any significant influence on the IRRAS while using the 4×4 matrix method from two different directions of observation.

Therefore, in order to develop the full anisotropic model for simulating the IRRAS spectra of SAMs, more investigations are required regarding the diagonalization of complex tensors. With the further investigation, the method can be established as an effective experimental tool to bridge the MD simulations with experimental measurement.

7.1 References

1. Parikh, A. N.; Allara, D. L., Quantitative determination of molecular structure in multilayered thin films of biaxial and lower symmetry from photon spectroscopies. I. Reflection infrared vibrational spectroscopy. *J. Chem. Phys.* **1992,** *96* (2), 927-945.
2. Teare, P., The crystal structure of orthorhombic hexatriacontane, $C_{36}H_{74}$. *Acta Cryst.* **1959,** *12* (4), 294-300.
3. Passler, N. C.; Paarmann, A., Generalized 4 × 4 matrix formalism for light propagation in anisotropic stratified media: study of surface phonon polaritons in polar dielectric heterostructures. *Opt. Soc. Am. B* **2017,** *34* (10), 2128-2139.
4. Passler, N. C.; Paarmann, A., Generalized 4 × 4 matrix formalism for light propagation in anisotropic stratified media: study of surface phonon polaritons in polar dielectric heterostructures: erratum. *J. Opt. Soc. Am. B* **2019,** *36* (11), 3246-3248.